



LAWRENCE
LIVERMORE
NATIONAL
LABORATORY

Cold Nuclear Matter Effects on J/psi and Upsilon Production at the LHC

R. Vogt

June 29, 2009

Physical Review C

Disclaimer

This document was prepared as an account of work sponsored by an agency of the United States government. Neither the United States government nor Lawrence Livermore National Security, LLC, nor any of their employees makes any warranty, expressed or implied, or assumes any legal liability or responsibility for the accuracy, completeness, or usefulness of any information, apparatus, product, or process disclosed, or represents that its use would not infringe privately owned rights. Reference herein to any specific commercial product, process, or service by trade name, trademark, manufacturer, or otherwise does not necessarily constitute or imply its endorsement, recommendation, or favoring by the United States government or Lawrence Livermore National Security, LLC. The views and opinions of authors expressed herein do not necessarily state or reflect those of the United States government or Lawrence Livermore National Security, LLC, and shall not be used for advertising or product endorsement purposes.

Cold Nuclear Matter Effects on J/ψ and Υ Production at the LHC

R. Vogt

*Lawrence Livermore National Laboratory,
Livermore, CA 94551, USA*

and

*Physics Department, University of California at Davis,
Davis, CA 95616, USA*

The charmonium yields are expected to be considerably suppressed if a deconfined medium is formed in high-energy heavy-ion collisions. In addition, the bottomonium states, with the possible exception of the $\Upsilon(1S)$ state, are also expected to be suppressed in heavy-ion collisions. However, in proton-nucleus collisions the quarkonium production cross sections, even those of the $\Upsilon(1S)$, scale less than linearly with the number of binary nucleon-nucleon collisions. These “cold nuclear matter” effects need to be accounted for before signals of the high density QCD medium can be identified in the measurements made in nucleus-nucleus collisions. We identify two cold nuclear matter effects important for midrapidity quarkonium production: “nuclear absorption”, typically characterized as a final-state effect on the produced quarkonium state and shadowing, the modification of the parton densities in nuclei relative to the nucleon, an initial-state effect. We characterize these effects and study their energy and rapidity dependence.

BASELINE TOTAL CROSS SECTIONS

To better understand quarkonium suppression, it is necessary to have a good estimate of the expected yields. However, there are still a number of unknowns about quarkonium production in the primary nucleon-nucleon interactions. In this section, we discuss models of quarkonium production and give predictions for the yields in a number of collision systems.

A	E_A (TeV)	y_A	$\sqrt{s_{NN}}$ (TeV)	y_{diff}^{pA}	$\Delta y_{\text{cm}}^{pA}$	$\sqrt{s_{NN}}$ (TeV)	y_{diff}^{dA}	$\Delta y_{\text{cm}}^{dA}$	$\sqrt{s_{NN}}$ (TeV)
			pA			dA			AA
O	3.5	8.92	9.9	0.690	0.345	7	0	0	7
Ar	3.15	8.81	9.39	0.798	0.399	6.64	0.052	0.026	6.3
Kr	3.07	8.79	9.27	0.824	0.412	6.48	0.077	0.038	6.14
Sn	2.92	8.74	9.0	0.874	0.437	6.41	0.087	0.043	5.84
Pb	2.75	8.67	8.8	0.934	0.467	6.22	0.119	0.059	5.5

TABLE I: For each ion species at the LHC, we give the maximum beam energy per nucleon and the corresponding beam rapidity. Using the maximum proton or deuteron beam energy: $E_p = 7$ TeV and $y_p = 9.61$; $E_d = 3.5$ TeV and $y_d = 8.92$ respectively, we present the maximum center-of-mass energy per nucleon; rapidity difference, $y_{\text{diff}}^{iA} = y_i - y_A$ ($i = p, d$); and center-of-mass rapidity shift, $\Delta y_{\text{cm}}^{iA} = y_{\text{diff}}^{iA}/2$, for pA , dA and AA collisions. Note that there is no rapidity shift in the symmetric AA case.

Since the LHC can collide either symmetric (AA) or asymmetric (AB) systems, we present results for pp , pA , dA and AA collisions. We consider dA collisions since the dA center-of-mass energy is closer to the AA collision energy than top energy pA collisions. The maximum ion beam energy per nucleon is the proton beam energy, $E_p = 7$ TeV, times the charge-to-mass ratio, Z/A , of the ion beam. Thus the maximum deuteron beam energy is half that of the proton beam, $E_d = 3.5$ TeV. The ion beam energies are given on the left-hand side of Table I for five reference nuclei: oxygen, $^{16}_8\text{O}$; argon, $^{40}_{18}\text{Ar}$; krypton, $^{84}_{36}\text{Kr}$; tin, $^{119}_{50}\text{Sn}$; and lead, $^{208}_{82}\text{Pb}$. Note that we use the average elemental A since a sample may contain an admixture of several isotopes of different A .

In addition to the AA center-of-mass energy, we also show the maximum pA and dA per nucleon center-of-mass energies, $\sqrt{s_{NN}} = \sqrt{4E_{p,d}E_A}$. Because $E_{p,d}$ is typically greater than E_A , the center-of-mass rapidity can shift away from $y = 0$. The total shift is $y_{\text{diff}}^{iA} = y_i - y_A$ ($i = p, d$) while the center of mass shifts by half this amount, $\Delta y_{\text{cm}}^{iA} = y_{\text{diff}}^{iA}/2$. Table I shows the maximum nucleon-nucleon center-of-mass energy per nucleon, the rapidity difference between the two beams, y_{diff}^{iA} , and the center-of-mass shifts for pA and dA collisions. (The Z/A ratio is the same for d and O thus $\Delta y^{dO} = 0$.) Only $\sqrt{s_{NN}}$ is given for symmetric AA collisions since there is no rapidity shift.

If there were no cold nuclear matter effects on the production cross sections at a given energy, the per nucleon cross sections would all be equal. However, the nuclear parton distributions (nPDFs) are known to be modified with respect to the free proton PDFs as a function of parton momentum fraction x . At low x , $x < 0.05$ (shadowing region), and high x , $x > 0.2$ (EMC region), the nuclear structure function, $F_2^A(x)$, the weighted sum of the charged parton distributions, is suppressed relative to that of the deuteron, $F_2^d(x)$, while, in the intermediate x region, the ratio $2F_2^A/AF_2^d$ is enhanced (antishadowing) in nuclear deep-inelastic scattering (nDIS). We refer to the modification of the parton densities in the nucleus as a function of A , x and μ^2 in general as shadowing. While a combination of nDIS and Drell-Yan data can separate the nuclear valence and sea quark densities, there is no direct probe of the nuclear gluon density.

Gluon fusion dominates quarkonium production over the entire accessible rapidity range at the LHC. Thus the nuclear gluon distribution, the most important for quarkonium studies, is unfortunately the most poorly measured. There are, however, a number of indirect constraints on the gluon density. The scale evolution of F_2^A and momentum conservation provide two important constraints. Most of the low- x nDIS data are at relatively low scales, below the minimum scale of a number of PDF sets and therefore less useful for studies of perturbative evolution. RHIC data on hadron production are an exception since intermediate p_T hadron production occurs at relatively low x and at perturbative scales. The BRAHMS forward charged hadron data [1] were used in the EPS08 fits to place an upper limit on the amount of possible gluon shadowing [2]. At relatively high x , the shape of the PHENIX midrapidity π^0 data [3] helps pin down the nuclear gluon density in the EMC region.

Quarkonium production occurs at sufficiently large scales to provide further constraints on the nuclear gluon PDFs. There are some drawbacks however: the quarkonium production mechanism is not fully understood, even in pp collisions, and the energy dependence of nuclear absorption is not well known. In the remainder of this section, we discuss the quarkonium yields in various collision systems; the implementation of modified PDFs for the nuclear parton densities; and quarkonium absorption by nucleons.

Early studies of high energy quarkonium production, particularly at high p_T , were performed in the context of the color singlet model (CSM) which calculates direct production of a quarkonium state with definite total spin, parity and charge conjugation. The CSM predicted that the χ_{c1} state, produced directly from gg fusion, would have a much larger cross section than direct color-singlet J/ψ production which requires a 3-gluon vertex [5]. Instead, measurements of direct J/ψ and χ_c production showed that the J/ψ cross section was, in fact, larger than the χ_c cross section [6]. However, the CSM can describe charmonium production in cleaner environments such as photoproduction [7] and more recent modifications of the CSM including s -channel cut diagrams can reproduce the J/ψ p_T distributions at RHIC and the Tevatron relatively well [8]. The different kinematics of the modified CSM probes larger values of x and thus reduces the shadowing effect [9].

Nonrelativistic QCD (NRQCD) is an effective field theory in which short-distance partonic interactions produce $Q\bar{Q}$ pairs in color singlet or color octet states which then evolve into a quarkonium state, as characterized by non-perturbative matrix elements [10]. The first term in the NRQCD expansion is equivalent to the CSM. The octet contributions are sufficient to explain the J/ψ yield at the Tevatron. However, the NRQCD approach has so far failed to describe quarkonium polarization [11].

Perhaps the simplest approach to quarkonium production is the color evaporation model (CEM) which treats heavy flavor and quarkonium production on an equal footing. The quarkonium production cross section is some fraction, F_C , of all $Q\bar{Q}$ pairs below the $H\bar{H}$ threshold where H is the lowest mass heavy-flavor hadron. Thus the CEM cross section is simply the $Q\bar{Q}$ production cross section with a cut on the pair mass but without any constraints on the color or spin of the final state. The color of the octet $Q\bar{Q}$ state is ‘evaporated’ through an unspecified process which does not change the momentum. The additional energy needed to produce heavy-flavored hadrons when the partonic center of mass energy, $\sqrt{\hat{s}}$, is less than $2m_H$, the $H\bar{H}$ threshold energy, is nonperturbatively obtained from the color field in the interaction region. Thus the quarkonium yield may be only a small fraction of the total $Q\bar{Q}$ cross section below $2m_H$. At leading order, the production cross section of quarkonium state C in an AB collision is

$$\begin{aligned} \frac{d\sigma_C^{\text{CEM}}(s_{NN})}{d^2r d^2b} &= F_C \sum_{i,j} \int_{4m_Q^2}^{4m_H^2} d\hat{s} \int dx_1 dx_2 \int dz' \\ &\times f_i^A(x_1, \mu^2, \vec{r}, z) f_j^B(x_2, \mu^2, \vec{b} - \vec{r}, z') \hat{\sigma}_{ij}(\hat{s}) \delta(\hat{s} - x_1 x_2 s_{NN}), \end{aligned} \quad (1)$$

where A and B can be any hadron or nucleus, $ij = q\bar{q}$ or gg and $\hat{\sigma}_{ij}(\hat{s})$ is the $ij \rightarrow Q\bar{Q}$ subprocess cross section. If one or both of the collision partners, A and B , is a proton, then the transverse, \vec{r} , and longitudinal, z , spatial parameters may be replaced by delta functions, $\int d^2r dz \delta(\vec{r}) \delta(z)$, and the parton densities are simply $f_i^A(x_1, \mu^2, \vec{r}, z) \equiv f_i^A(x_1, \mu^2)$. Our calculations use the NLO $Q\bar{Q}$ code of Mangano *et al.* [15] with the $2m_H$ mass cut in Eq. (1), as described in Ref. [12] and use the same parameters as in Refs. [13, 14].

To go beyond pp collisions, the proton parton densities must be replaced by those of the nucleus. Then the collision geometry and the spatial dependence of the shadowing parameterization also need to be considered. We assume that if A is a nucleus, the nuclear parton densities, $f_i^A(x_1, \mu^2, \vec{r}, z)$, factorize into the nucleon density in the nucleus, $\rho_A(\vec{r}, z)$, independent of the kinematics; the nucleon parton density, $f_i^p(x_1, \mu^2)$, independent of A ; and a shadowing ratio, $S_{P,S}^i(A, x_1, \mu^2, \vec{r}, z)$ that parameterizes the modifications of the nucleon parton densities in the nucleus. The first subscript, P, refers to the choice of shadowing parameterization, while the second, S, refers to the spatial dependence. Thus,

$$f_i^A(x_1, \mu^2, \vec{r}, z) = \rho_A(s) S_{P,S}^i(A, x_1, \mu^2, \vec{r}, z) f_i^p(x_1, \mu^2), \quad (2)$$

$$f_j^B(x_2, \mu^2, \vec{b} - \vec{r}, z') = \rho_A(s') S_{P,S}^j(B, x_2, \mu^2, \vec{b} - \vec{r}, z') f_j^p(x_2, \mu^2), \quad (3)$$

where $s = \sqrt{r^2 + z^2}$ and $s' = \sqrt{|\vec{b} - \vec{r}|^2 + z'^2}$.

The nucleon densities of the heavy nucleus are assumed to be Woods-Saxon distributions with $R_{Au} = 6.38$ fm and $R_{Pb} = 6.62$ fm [16] and are normalized so that $\int d^2r dz \rho_A(s) = A$. With no nuclear modifications, $S_{P,S}^i(A, x, Q^2, \vec{r}, z) \equiv 1$ and integration of the nuclear parton densities over the spatial variables gives

$$\int d^2b d^2s dz dz' f_i^A(x_1, \mu^2, \vec{r}, z) f_j^B(x_2, \mu^2, \vec{b} - \vec{r}, z') = AB f_i^p(x_1, \mu^2) f_j^p(x_2, \mu^2). \quad (4)$$

The impact-parameter averaged shadowing parameterization measured in nDIS is recovered by integrating $S_{P,S}$ over the volume, weighted by the nuclear density,

$$\frac{1}{A} \int d^2r dz \rho_A(s) S_{P,S}^i(A, x, \mu^2, \vec{r}, z) = S_P^i(A, x, \mu^2). \quad (5)$$

We discuss more details of the spatial dependence of $S_{P,S}$ in Section 2.3. Most available shadowing parameterizations, including the ones used here, ignore the small effects in deuterium. However, we take the proton and neutron numbers of both nuclei into account. The impact-parameter integrated up and down quark distributions, needed for the $q\bar{q}$ contribution to quarkonium production, are calculated as

$$f_q^A(x, \mu^2) = (Z_A S_{P,p}^q(A, x, \mu^2) f_q^p(x, \mu^2) + N_A S_{P,n}^q(A, x, \mu^2) f_q^n(x, \mu^2)) \quad (6)$$

for $q = u$ and d , assuming that, as for the proton and neutron parton densities, $S_{P,n}^u = S_{P,p}^d$ and $S_{P,n}^d = S_{P,p}^u$ and similarly for the antiquarks.

To obtain the rapidity distribution from the total cross section, an additional delta function, $\delta(y - 0.5 \ln(x_1/x_2))$, is included in Eq. (1). At leading order, the parton momentum fractions x_1 and x_2 are simply $x_{1,2} = (\sqrt{\hat{s}/s_{NN}}) \exp(\pm y)$. In this notation then, in the forward rapidity region of a pA collision, x_1 , the proton momentum fraction, is larger and x_2 , the parton momentum fraction in the nucleus, is smaller than the midrapidity value, $x = \sqrt{\hat{s}/s_{NN}}$.

Some of the uncertainties in the production model may be overcome by studying ratios, *e.g.* pA/pp , at the same center-of-mass energy since the dominance of gg processes means that the pA/pp ratio is, to a good approximation, the ratio of the gluon distribution in the nucleus relative to the gluon distribution in the proton. We have chosen to use the CEM because it allows predictions of the total cross section and the p_T -integrated rapidity distributions where nuclear effects are more prominent. Measuring the J/ψ and Υ ratios simultaneously also provides a means of determining the scale evolution of the nuclear gluon distribution at relatively large, perturbative scales if shadowing is the only cold nuclear matter effect in pA and dA collisions.

At fixed-target energies, the x_F dependence clearly shows that shadowing is not the only contribution to the J/ψ nuclear dependence as a function of x_F [17, 20]. Indeed, the characteristic decrease of $\alpha(x_F)$ for $x_F \geq 0.25$, cannot be explained by shadowing alone [21]. In fact, the data so far demonstrate scaling with x_F , not the target momentum fraction x_2 [22], in contradiction to perturbative QCD factorization, indicating the possible importance of higher-twist effects [23]. The preliminary PHENIX data show an increasing suppression at forward rapidity [24], similar to that seen in fixed-target experiments at large x_F .

Effects we have not considered here which may result in x_F rather than x_2 scaling and affect the high x_F region are energy loss in cold matter and intrinsic charm, both discussed extensively in Ref. [21]. We do not consider these effects here because, at heavy-ion colliders, the relationship between x_F , rapidity, and $\sqrt{s_{NN}}$ suggests that this interesting x_F region is pushed to far forward rapidities. The onset of initial-state energy loss should, in fact, appear at higher x_F at larger $\sqrt{s_{NN}}$ if it depends on the momentum fraction x_1 . Figure 1 shows the relationship between x_F and

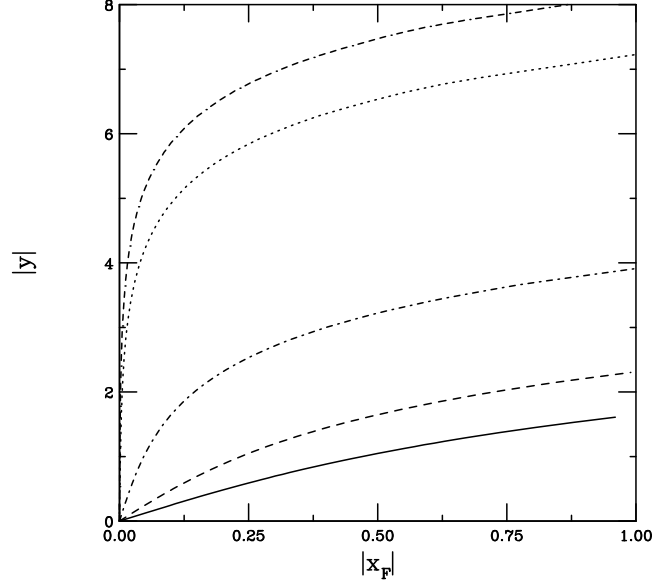


FIG. 1: For $M = 4$ and $\sqrt{s_{NN}} = 20$ (solid), 40 (dashed), 200 (dot-dashed), 5500 (dotted) and 14000 (dot-dot-dot-dashed) GeV, we give the average value of the center-of-mass rapidity, y , in pp collisions as a function of x_F . Note the absolute values on y and x_F : in the center-of-mass frame, $|x_F| < 1$ and $|y| \leq y_{\max}$ so that the curves shown here are diagonally reflected around $x_F = y = 0$.

y in the center-of-mass frame for $M = 4$ GeV and $20 \leq \sqrt{s_{NN}} \leq 14000$ GeV. Since $x_F = (2m_T/\sqrt{s_{NN}}) \sinh y$, the large center-of-mass energies at the LHC guarantees that the forward x_F region will not be accessible in the central rapidity region of the LHC. Instead, the x_F distribution becomes narrowly peaked with increasing energy while the rapidity distribution becomes broad and flat. At $y = 5$, the largest x_F accessible (at the lowest $\sqrt{s_{NN}}$) is 0.081 for the J/ψ and 0.25 for the Υ . The large x_F region is therefore not probed by quarkonium production in $|y| \leq 5$. Thus shadowing and absorption are likely the most important cold nuclear matter effects at the LHC.

To implement nuclear absorption on quarkonium production in pA and dA collisions, the production cross section is weighted by the survival probability, S_C^{abs} , so that

$$S_C^{\text{abs}}(\vec{b} - \vec{s}, z') = \exp \left\{ - \int_{z'}^{\infty} dz'' \rho_A(\vec{b} - \vec{s}, z'') \sigma_{\text{abs}}^C(z'' - z') \right\} \quad (7)$$

where z' is the longitudinal production point, as in Eq. (3), and z'' is the point at which the state is absorbed. The nucleon absorption cross section, σ_{abs}^C , typically depends on the spatial location at which the state is produced and how far it travels through the medium. If absorption alone is active, *i.e.* $S_{\text{P},S}^i(A, x, \mu^2, \vec{r}, z) \equiv 1$, then an effective minimum bias A dependence is obtained after integrating Eqs. (1) and (7) over the spatial coordinates. If $S_C^{\text{abs}} = 1$ also, $\sigma_{pA} \approx A \sigma_{pp}$ without any cold nuclear matter effects. (Note that for gg -dominated processes, such as quarkonium production, the relationship would be exact. When qq' or $q\bar{q}'$ interactions dominate, as in gauge boson production, the different relative proton and neutron numbers make the above relationship approximate.) If $S_{\text{P},S}^i(A, x, \mu^2, \vec{r}, z) \equiv 1$ and $S_C^{\text{abs}} \neq 1$, $\sigma_{pA} = A^\alpha \sigma_{pp}$ where the exponent α can be related to the absorption cross section, as studied in detail for J/ψ and ψ' production by NA50 [25]. For a constant σ_{abs}^C with a sharp surface spherical nucleus of density $\rho_A = \rho_0 \theta(R_A - b)$, it can be shown that

$$\alpha = 1 - \frac{9\sigma_{\text{abs}}^C}{16\pi r_0^2} \quad (8)$$

where $r_0 = 1.2$ fm [26]. The relationship between α and σ_{abs}^C is less straightforward in more realistic geometries.

The NA50 [25] and E866 [17] experiments measured a non-negligible difference in the effective J/ψ and ψ' absorption cross sections at $\sqrt{s_{NN}} = 23 - 29$ GeV and $\sqrt{s_{NN}} = 38.8$ GeV respectively. In addition, the difference between $\sigma_{\text{abs}}^{J/\psi}$ and $\sigma_{\text{abs}}^{\psi'}$ seems to decrease with $\sqrt{s_{NN}}$. This shows that absorption must be a final-state effect since an initial-state effect such as shadowing would not discriminate between the asymptotic J/ψ and ψ' final states. Comparing the effective absorption cross sections determined at central rapidities from the CERN SPS to RHIC, absorption seems to decrease with energy [27].

Fewer Υ pA data are available. The E772 experiment [18] measured the A dependence of the three S states and found a reduced A dependence relative to J/ψ absorption. The A dependence of the three S states was indistinguishable within the uncertainties. No Υ A dependence was presented by the E866 collaboration. The STAR d+Au/ pp ratio suggests that, at RHIC, the Υ A dependence is linear [19]. Thus absorption seems to be weaker overall for Υ production but there is not clear indication so far of how much weaker it is or whether it has the same energy dependence as J/ψ .

If conventional shadowing parameterizations, such as the ones used in this paper, are included, the effective absorption cross section may seem to decrease with energy due to the increased effect of shadowing at low x . A decrease in absorption concurrent with increased shadowing as $\sqrt{s_{NN}}$ increases seems to approximately hold, even without shadowing, at fixed-target energies [27]. Such a decrease is consistent with the J/ψ traversing the nucleus as a color singlet. If the nuclear crossing time is shorter than the J/ψ formation time, the effective absorption decreases with $\sqrt{s_{NN}}$ as an ever smaller state passes through the target.

If the effective absorption cross section indeed decreases with energy, then absorption should be a relatively small contribution to the total A dependence at the LHC. This prediction is easy to check: if absorption is negligible, the J/ψ and ψ' pA/pp ratios should depend only on shadowing and should thus be equivalent. The yield is then related to the ratio of the nuclear to proton gluon densities since gg fusion dominates quarkonium production at these energies. In this work, we have assumed that absorption is negligible so that the pA/pp , dA/pp and AA/pp J/ψ and Υ ratios presented here are the same for all charmonium and bottomonium states respectively.

If both the pA and pp data are taken at the same $\sqrt{s_{NN}}$, the same x values of the gluon densities will be probed in the nucleus and in the proton. Such same energy comparison runs would be an excellent probe of the nuclear gluon distributions because

$$\frac{pA(\sqrt{s_{NN}})}{pp(\sqrt{s_{NN}})} \propto \frac{f_g^A(x, \mu^2)}{f_g^p(x, \mu^2)}. \quad (9)$$

However, if the pA and pp data are recorded at different energies (and x values), the extraction of the nuclear gluon density is less straightforward since

$$\frac{pA(\sqrt{s_{NN}})}{pp(\sqrt{s})} \propto \frac{f_g^A(x', \mu^2)}{f_g^p(x, \mu^2)}. \quad (10)$$

In both cases, the p_T -integrated ratios provide an additional uncertainty because the scale evolution of the gluon density is not well known but is expected to be strong [2, 28–31]. However, the quarkonium p_T distribution is steeply falling for $p_T \geq m$ so that the p_T -integrated ratios are a good representation of $\mu^2 = \langle m_T \rangle^2$.

The scale evolution of the gluon densities can be probed in part by relative studies of low p_T or p_T -integrated J/ψ ($m_\psi = 3.097$ GeV) and $\Upsilon(1S)$ ($m_{\Upsilon(1S)} = 9.46$ GeV) production. To more precisely obtain the scale evolution of shadowing, it would be preferable to bin the J/ψ and $\Upsilon(1S)$ pA/pp ratios in p_T . One must be careful in the interpretation of such ratios, particularly at $p_T < m$, since, at fixed-target energies, the p_T -dependent pA/pp ratios show that the J/ψ and Υ p_T distributions are broader in pA than in pp interactions [32, 33]. This broadening has been attributed to intrinsic parton p_T kicks accrued by the interacting parton as it traverses the nucleus before interacting [34, 35]. The magnitude of the average p_T kick increases with A so that the p_T -dependent pA/pp ratio is less than unity at low p_T and increases above one with increasing p_T . This effect is important at low center-of-mass energies where the average p_T of the produced quarkonium state is not large. By LHC energies, while the p_T kick may be rather small relative to $\langle p_T^2 \rangle$, it may still affect the analysis of shadowing effects in p_T -binned ratios but not in p_T -integrated ratios. We focus on the p_T -integrated results here and will present p_T -dependent calculations elsewhere.

As an example of the possible cross sections for quarkonium production at the LHC, we present the total cross sections in pp , pA , dA and AA collisions at the relevant energies. To illustrate the effects of shadowing on the total cross section, calculated to next-to-leading order in the CEM [12], we use the EKS98 parameterization [28, 29]. For each possible maximum pA , dA and AA center-of-mass energy, we also give the pp cross section at that same energy. In addition, for the AA center-of-mass energies, we also give the pp and pA cross sections at that energy. The results are given in Tables II and III. The central columns are the direct cross sections per nucleon pair for all charmonium and bottomonium states. The effects are largest for charmonium (lower x and μ^2 than the Υ states) and for the heaviest nuclei (lowest energies – highest x – but largest A). On the right-hand side of the tables, the inclusive (direct plus feed down) cross sections are multiplied by the dilepton decay branching ratios. They are also multiplied by AB to obtain the minimum bias total cross sections.

The approximate A dependence of the total cross section relative to the pp cross section at the same center-of-mass

		$\sigma^{\text{dir}}/\text{nucleon pair } (\mu\text{b})$				$B\sigma^{\text{inc}} AB (\mu\text{b})$	
System	$\sqrt{s_{NN}}$ (TeV)	J/ψ	χ_{c1}	χ_{c2}	ψ'	J/ψ	ψ'
pp	14	32.9	31.8	52.5	7.43	3.15	0.055
pp	10	26.8	26.0	43.3	6.06	2.57	0.044
pp	9.9	26.6	25.8	42.6	6.02	2.55	0.044
$p\text{O}$	9.9	23.8	23.0	38.0	5.37	36.5	0.632
pp	9.39	25.8	25.0	41.3	5.83	2.48	0.043
$p\text{Ar}$	9.39	22.0	21.2	35.1	4.96	84.1	1.46
pp	9.27	25.6	24.8	40.9	5.79	2.46	0.043
$p\text{Kr}$	9.27	20.9	20.2	33.4	4.73	168.4	2.92
pp	9	25.2	24.4	40.2	5.69	2.41	0.042
$p\text{Sn}$	9	20.2	19.6	32.3	4.56	230.4	3.99
pp	8.8	25.0	24.2	39.9	5.65	2.40	0.042
$p\text{Pb}$	8.8	19.5	18.9	31.1	4.40	388.8	6.75
pp	7	21.8	21.1	34.9	4.93	2.09	0.036
$p\text{O}$	7	19.5	19.0	31.3	4.42	30.0	0.520
$d\text{O}$	7	19.5	19.0	31.3	4.42	60.0	1.04
$\text{O}+\text{O}$	7	17.6	17.0	28.1	3.98	432.4	7.51
pp	6.64	21.2	20.5	33.8	4.78	2.02	0.035
$d\text{Ar}$	6.64	18.1	17.5	28.9	4.09	138.5	2.39
pp	6.48	20.9	20.2	33.3	4.71	2.00	0.034
$d\text{Kr}$	6.48	17.2	16.6	28.0	3.95	281.3	4.85
pp	6.41	20.7	20.1	33.1	4.68	1.98	0.034
$d\text{Sn}$	6.41	16.8	16.2	26.8	3.78	378.3	6.52
pp	6.3	20.5	19.9	32.8	4.63	1.97	0.034
$p\text{Ar}$	6.3	17.6	17.0	28.1	3.97	67.3	1.17
$\text{Ar}+\text{Ar}$	6.3	15.0	14.5	23.9	3.38	2300	40.0
pp	6.22	20.4	19.7	32.5	4.60	1.95	0.34
$d\text{Pb}$	6.22	16.0	15.5	25.6	3.62	637.3	10.98
pp	6.14	20.2	19.6	32.3	4.56	1.94	0.034
$p\text{Kr}$	6.14	16.6	16.1	26.6	3.76	134.0	2.32
$\text{Kr}+\text{Kr}$	6.14	13.7	13.2	21.8	3.08	9245	160.6
pp	5.84	19.6	19.0	31.3	4.42	1.88	0.033
$p\text{Sn}$	5.84	15.9	15.4	25.4	3.59	181.3	3.14
$\text{Sn}+\text{Sn}$	5.84	12.8	12.4	20.4	2.89	17391	302.0
pp	5.5	18.9	18.3	30.2	4.26	1.81	0.032
$p\text{Pb}$	5.5	14.9	14.4	23.8	3.37	297.6	5.16
$\text{Pb}+\text{Pb}$	5.5	11.7	11.3	18.7	2.64	48500	842

TABLE II: The direct cross section per nucleon pair (central columns) and the dilepton yield per nucleon multiplied by AB . The results are given for the MRST PDFs with $m_c = 1.2$ GeV, $\mu_F = \mu_R = 2m_T$.

energy, assuming no other cold matter effects, can be obtained from the $(AB)^\alpha$ parameterization so that, per nucleon,

$$\alpha(pA/pp) \sim 1 + \frac{\ln[f_g^A(x'_2, \mu^2)/f_g^p(x_2, \mu^2)]}{\ln A} \quad (11)$$

$$\alpha(AB/pp) \sim 1 + \frac{\ln[f_g^A(x'_1, \mu^2)f_g^B(x'_2, \mu^2)/(f_g^p(x_1, \mu^2)f_g^p(x_2, \mu^2))]}{\ln(AB)} \quad (12)$$

where $x'_2 = x_2$ and $x'_1 = x_1$ if the center-of-mass energies are the same for the two systems. For J/ψ production in $p\text{Pb}$ and $\text{Pb}+\text{Pb}$ collisions relative to pp collisions at 5.5 TeV, $\alpha \sim 0.76$ and 0.52 respectively. In the case of Υ production, we have $\alpha \sim 0.88$ and 0.76 respectively.

System	$\sqrt{s_{NN}}$ (TeV)	$\sigma^{\text{dir}}/\text{nucleon pair } (\mu\text{b})$					$B\sigma^{\text{inc}} AB (\mu\text{b})$		
		Υ	Υ'	Υ''	$\chi_b(1P)$	$\chi_b(2P)$	Υ	Υ'	Υ''
pp	14	0.43	0.27	0.16	0.89	0.69	0.020	0.0074	0.0036
pp	10	0.33	0.21	0.12	0.70	0.54	0.016	0.0059	0.0028
pp	9.9	0.32	0.20	0.12	0.66	0.51	0.015	0.0055	0.0026
$p\text{O}$	9.9	0.30	0.19	0.11	0.62	0.48	0.23	0.082	0.040
pp	9.39	0.30	0.19	0.12	0.63	0.49	0.014	0.0052	0.0025
$p\text{Ar}$	9.39	0.28	0.17	0.11	0.57	0.44	0.53	0.19	0.092
pp	9.27	0.30	0.19	0.11	0.62	0.48	0.014	0.0052	0.0025
$p\text{Kr}$	9.27	0.27	0.17	0.10	0.55	0.43	1.06	0.39	0.19
pp	9	0.29	0.18	0.11	0.61	0.47	0.014	0.0050	0.0024
$p\text{Sn}$	9	0.26	0.16	0.099	0.53	0.42	1.46	0.53	0.26
pp	8.8	0.29	0.18	0.11	0.60	0.47	0.014	0.0059	0.0024
$p\text{Pb}$	8.8	0.25	0.16	0.097	0.52	0.41	2.51	0.96	0.45
pp	7	0.23	0.15	0.090	0.48	0.38	0.011	0.0043	0.0019
$p\text{O}$	7	0.22	0.14	0.085	0.46	0.36	0.17	0.061	0.029
$d\text{O}$	7	0.22	0.14	0.085	0.46	0.36	0.34	0.12	0.058
$\text{O}+\text{O}$	7	0.21	0.13	0.081	0.44	0.34	2.57	0.97	0.46
pp	6.64	0.22	0.14	0.085	0.46	0.36	0.011	0.0038	0.0019
$d\text{Ar}$	6.64	0.20	0.13	0.079	0.42	0.33	0.78	0.27	0.13
pp	6.48	0.22	0.14	0.083	0.45	0.35	0.010	0.0037	0.0018
$d\text{Kr}$	6.48	0.20	0.12	0.076	0.41	0.32	1.57	0.56	0.28
pp	6.41	0.21	0.14	0.082	0.44	0.35	0.010	0.0036	0.0018
$d\text{Sn}$	6.41	0.19	0.12	0.074	0.40	0.34	2.34	0.77	0.41
pp	6.3	0.21	0.14	0.082	0.44	0.34	0.010	0.0038	0.0018
$p\text{Ar}$	6.3	0.20	0.12	0.075	0.41	0.32	0.37	0.13	0.065
$\text{Ar}+\text{Ar}$	6.3	0.18	0.12	0.070	0.38	0.29	13.8	5.29	2.43
pp	6.22	0.21	0.13	0.080	0.43	0.34	0.010	0.0035	0.0017
$d\text{Pb}$	6.22	0.18	0.12	0.071	0.38	0.30	3.68	1.31	0.65
pp	6.14	0.21	0.13	0.080	0.43	0.33	0.0099	0.0038	0.0017
$p\text{Kr}$	6.14	0.19	0.12	0.072	0.39	0.30	0.75	0.27	0.13
$\text{Kr}+\text{Kr}$	6.14	0.17	0.11	0.066	0.35	0.28	57.4	21.8	10.1
pp	5.84	0.20	0.12	0.076	0.41	0.32	0.0094	0.0035	0.0017
$p\text{Sn}$	5.84	0.18	0.11	0.068	0.37	0.29	1.01	0.36	0.18
$\text{Sn}+\text{Sn}$	5.84	0.16	0.10	0.062	0.33	0.26	108.1	41.3	19.0
pp	5.5	0.19	0.12	0.070	0.39	0.30	0.0090	0.0029	0.0016
$p\text{Pb}$	5.5	0.17	0.11	0.064	0.34	0.27	1.65	0.60	0.29
$\text{Pb}+\text{Pb}$	5.5	0.15	0.094	0.057	0.31	0.24	304	116.1	53.5

TABLE III: The direct cross section per nucleon pair (central columns) and the dilepton yield per nucleon multiplied by AB . The results are given for the MRST PDFs with $m_b = 4.75$ GeV, $\mu_F = \mu_R = m_T$.

The pp rapidity distributions for J/ψ and Υ production at $\sqrt{s_{NN}} = 5.5$ and 14 TeV are compared to RHIC distributions at $\sqrt{s_{NN}} = 200$ and 500 GeV in Fig. 2. The LHC distributions are relatively constant over a range of 5 or more units of rapidity, demonstrating that the cross sections are high enough to obtain good statistics for quarkonium states, even for forward production and detection, provided that the decay leptons are of sufficiently high p_T to reach the detectors¹.

¹ This will be more difficult for CMS and ATLAS than for ALICE since the minimum muon p_T for detection in the large pp experiments

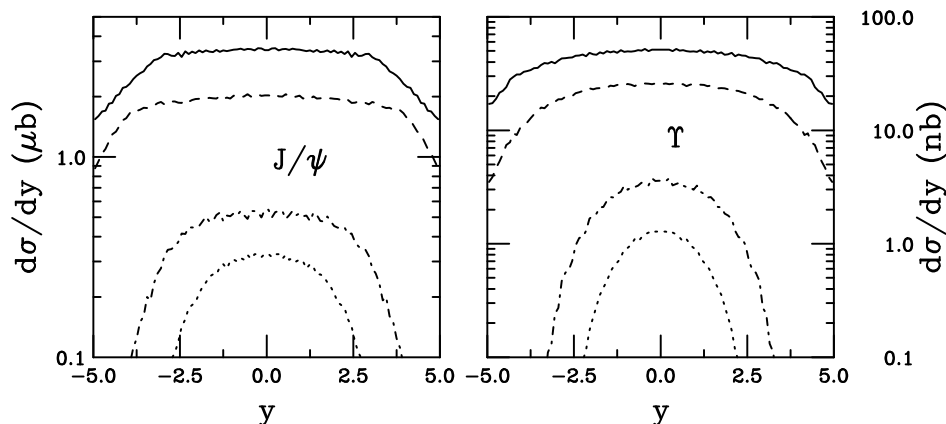


FIG. 2: The J/ψ (left-hand side) and Υ (right-hand side) rapidity distributions at $\sqrt{s_{NN}} = 200$ (dotted), 500 (dot-dashed), 5500 (dashed) and 14000 (solid) GeV. The kinks in the J/ψ distributions at LHC energies are the point where $x < 10^{-5}$. Since the Υ factorization scale is larger, their distributions are smooth as a function of rapidity. Note the different scales on the y -axes.

COLD NUCLEAR MATTER EFFECTS

We now show predictions of the J/ψ and Υ production ratios as a function of rapidity for cold nuclear matter, CNM, effects at the LHC. If hA data (where $h = p$ or d) can be taken at the same energy as the pp and/or AA data, as at RHIC, it is easier to make comparisons. However, the setup of the LHC makes this ideal situation more difficult. At the nominal injection energy, the proton beam has an energy of 7 TeV while the nuclear beam energy per nucleon is lower by the nuclear charge-to-mass ratio, Z/A . To make a pp comparison, if we are not to rely on calculations extrapolated to lower energy, the pp collisions have to be run at the pA or AA per nucleon energies. For the proton and ion beam energies to be the same, the proton beam must then circulate at lower than optimal energy, decreasing the luminosity. Since sustained low energy pp runs are unlikely in early LHC running, especially for sufficiently accurate quarkonium data as a function of rapidity, it may be necessary to rely on 10 and 14 TeV pp reference data². However, there is a catch. In pA collisions where a 7 TeV proton beam collides with a $7(Z/A)$ TeV per nucleon ion beam, the so-called equal-speed frame, the center-of-mass rapidity is not fixed at $y = 0$ but displaced by Δy_{cm}^{iA} . In pPb collisions, the shift can be nearly 0.5 units, an important difference, see Table I for the magnitude of the possible shifts. To minimize the rapidity shift and to bring the hA comparison energy closer to that of the AA energy, dA collisions may be desirable since $E_d = 3.5$ TeV per nucleon relative to $E_{Pb} = 2.75$ TeV, see Table I. Since dA collisions require a second ion source, this is not a short term solution.

We thus study several different possibilities for determining cold nuclear matter effects on nucleus-nucleus collisions at the LHC. We go from ideal to more realistic scenarios. We first show pA/pp ratios at the same per nucleon center-of-mass energy for both systems, assuming the appropriate pp energies are available. In the case where pA and pp interactions are compared at the AA energy, we assume zero rapidity gap, $\Delta y_{cm}^{pA} = 0$, between the colliding beams since the proton beam energy is reduced to match that of the nucleus. In the more likely scenario, the pA data will be taken in the equal-speed frame at a higher energy than the AA collisions. Therefore, we next show the pA/pp ratios with respect to pp collisions at $\sqrt{s} = 14$ TeV with $\Delta y_{cm}^{pA} = 0$ for pA collisions both in the equal-speed frame and at the AA center-of-mass energy. The final pA calculations shown are the most realistic: the pA cross section in the equal-speed frame with finite Δy_{cm}^{pA} is shown relative to the pp cross section at 14 TeV. In this case, the numerator and denominator are calculated with different energies and different center-of-mass rapidities. Next, dA/pp ratios are presented for two cases: with the dA and pp collisions at the dA center-of-mass energy and with dA collisions in the equal-speed frame with $\Delta y_{cm}^{dA} \neq 0$ and pp collisions at 14 TeV. Finally, we present the baseline AA/pp ratios with the pp center-of-mass energy tuned to the AA energy and at the nominal 14 TeV pp energy. In the case of symmetric pp and AA collisions, there is no rapidity gap.

¹ is 3.5 GeV/c.

² The startup LHC pp run will be at 10 TeV. Thus we also provide the quarkonium cross sections at 10 TeV but show most of our results relative to the maximum pp energy of 14 TeV.

Shadowing parameterizations

We use several parameterizations of the nuclear modifications in the parton densities to probe the possible range of gluon shadowing effects: EKS98 [28, 29], nDSg [30], HKN [31], EPS08 [2] and EPS09 [4]. All sets involve fits to data, typically nDIS data with additional constraints from other observables such as Drell-Yan dimuon production. Since these provide no direct constraint on the nuclear gluon density, it is obtained through fits to the μ^2 dependence of the nuclear structure function, F_2^A , and momentum conservation. The useful perturbative μ^2 range of the nDIS data is rather limited since these data are only available at fixed-target energies. Thus the reach in momentum fraction, x , is also limited and there is little available data for $x < 10^{-2}$ at perturbative values of μ^2 . This situation is likely not to improve until an eA collider is constructed [36].

The EKS98 parameterization, by Eskola and collaborators, available for $A > 2$, is a leading order fit using the GRV LO [37] proton parton densities as a baseline [28, 29]. The kinematic range is $2.25 \leq \mu_{\text{EKS98}}^2 \leq 10^4 \text{ GeV}^2$ and $10^{-6} \leq x < 1$. deFlorian and Sassot produced the nDS and nDSg parameterizations [30] at both leading and next-to-leading order for $4 < A < 208$. The weak gluon shadowing of the nDS parameterization appears to be ruled out by the rapidity dependence of J/ψ production at RHIC [38]. The stronger gluon shadowing of nDSg is used here. Calculations with the nDS parameterization predict negligible shadowing effects. The kinematic reach in x is the same as EKS98 while the μ^2 range is larger, $1 < \mu_{\text{nDSg}}^2 < 10^6 \text{ GeV}^2$. Hirai and collaborators produced the leading order HKN parameterization by fitting parton densities for protons, deuterons and 16 heavier nuclei, typically those most commonly used in nDIS experiments. If a particular value of A needed for our calculations is not included, a set with a similar value of A is substituted. The HKN parameterization goes lower in x than the other parameterizations, $10^{-9} < x < 1$, and higher in scale, $1 < \mu_{\text{HKN}}^2 < 10^8 \text{ GeV}^2$. The EPS08 parameterization is a fit by Eskola and collaborators that includes the BRAHMS d+Au data on forward rapidity hadron production at RHIC [1] designed to maximize the possible gluon shadowing. Its x range is the same as EKS98, $10^{-6} \leq x < 1$, while the μ^2 range has been extended, $1.96 \leq \mu_{\text{EPS08}}^2 \leq 10^6 \text{ GeV}^2$. Very recently, the EPS09 [4] parameterization was introduced. EPS09 includes uncertainties on the global analyses, both at LO and NLO. Their central results are in quite good agreement with the EKS98 parameterization while the maximum possible gluon shadowing obtained in their uncertainty is similar to the EPS08 gluon ratio. The minimal amount of gluon shadowing is nearly negligible, similar to nDS [30]. We present the central EPS09 ratio as well as the ratios corresponding to the maximum and minimum range of the shadowing effect, obtained by adding the relative differences in quadrature, as prescribed in Ref. [4]. For computational convenience, we use the LO version of the nPDF parameterizations since the NLO CEM calculations give similar shadowing results [39]. This is to be expected since, even though the LO and NLO values of the cross section and the shadowing parameterization are different, when convoluted, they give the same ratios by design, see *e.g.* Ref. [30].

While the x values probed at midrapidity are $\approx 10^{-4}$ for the J/ψ and $\approx 10^{-3}$ for the Υ , well within the x range of the parameterizations, this is not necessarily the case away from midrapidity. At the largest values of $\sqrt{s_{NN}}$, x values lower than the minimum valid x of the parameterization may be reached within the rapidity range of the LHC detectors. In these cases, the shadowing parameterizations are unconstrained.

The ratios of the nuclear gluon densities relative to the gluon density in the proton are shown in Fig. 3 for four different ion species available at the LHC: $A = \text{O, Ar, Sn and Pb}$. The calculations for $A = \text{Kr}$, an alternative intermediate mass ion species, are not shown. Results for scales appropriate for J/ψ and Υ production are shown on the left and right-hand sides respectively, thus illustrating the scale dependence of the parameterizations. The scales correspond to those used in the calculations of the cross sections in Tables II and III with $\mu = 2m_c$ for charm and m_b for bottom respectively. If a lower scale, $\mu = m_c$, is used for charm, the shadowing effect is stronger since μ^2 is then closer to the minimum scale of the parameterization. Note that in all cases shadowing increases with decreasing x and increasing A while decreasing with scale, μ , as seen by comparing the left and right-hand sides of Fig. 3. For example, the EKS98, nDSg and HKN ratios appear to be approximately independent of x for $x < 10^{-3}$ at the J/ψ scale but not at the Υ scale.

The EKS98, EPS08 and EPS09 parameterizations (solid and dotted curves and solid curves with symbols respectively) exhibit large antishadowing, $S^g > 1$, in the region $0.02 < x < 0.2 - 0.3$, becoming more pronounced for larger A . The nDSg parameterization (dashed curves) show very weak antishadowing around $x \sim 0.1$. At $x < 10^{-2}$, it is weakest for $A = \text{O and Ar}$, similar to HKN for $A = \text{Sn}$ and compatible with EKS98 for $x < 10^{-3}$. The HKN parameterization (dot-dashed curves), on the other hand, is similar to EKS98 for $A = \text{O}$ but has a weak A dependence so that HKN shadowing is the weakest at low x and large A . The EPS08 parameterization is similar to EKS98 for $x > 0.01$ but exhibits stronger antishadowing at large A . It also has the strongest shadowing at low x since the low- p_T forward-rapidity BRAHMS data was included in the fit. The scale dependence of nDSg and HKN appears to be weaker than EKS98. The EPS09 band is obtained by calculating the deviations from the central value for the 15

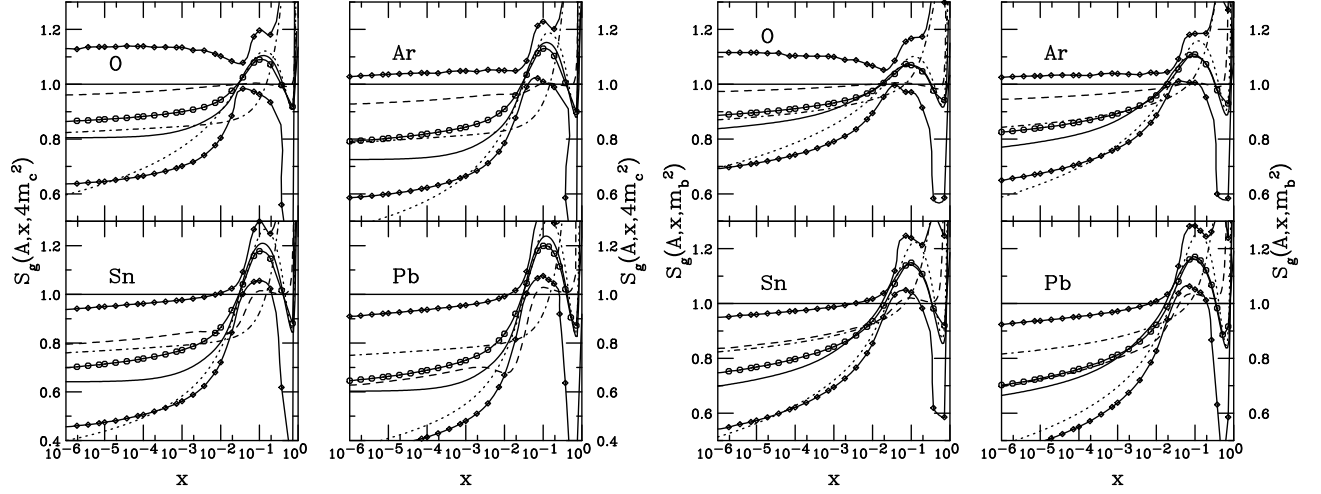


FIG. 3: The LO shadowing parameterizations for J/ψ (left) and Υ (right) scales for O (upper left), Ar (upper right), Sn (lower left) and Pb (lower right) nuclei. The parameterizations are EKS98 (solid), nDSg (dashed), HKN (dot-dashed), EPS08 (dotted) and EPS09 (solid lines with symbols). Note that the lower limit on the y -axis is changed for Sn and Pb on the left-hand side.

parameter variations on either side of the central set and adding them in quadrature. The range of the LO EPS09 uncertainty band encompasses all other shadowing ratios, similar to EPS08 for the maximum effect and even leading to antishadowing for lighter ions. (The central ratio is shown with circular symbols on the solid curve while the bounds include diamond symbols.) For smaller nuclei, the upper edge of the EPS09 uncertainty (minimal shadowing effect) gives a bound above unity for S^g .

All the parameterizations increase at large x with $S^g > 1$ for $x > 0.1$ (HKN and nDSg) and $x > 0.7$ (EKS98 and EPS08). The rise in the HKN parameterization is steepest and occurs at the lowest x , beginning at the x value of the antishadowing peak in the EKS98 and EPS08 ratios. This high x region will not be explored by the LHC detectors since it is only reached at rapidities outside their acceptance.

Finally, we note that since our pA calculations assume the ion beam comes from the right, low x corresponds to large forward rapidity while high x corresponds to large backward rapidity.

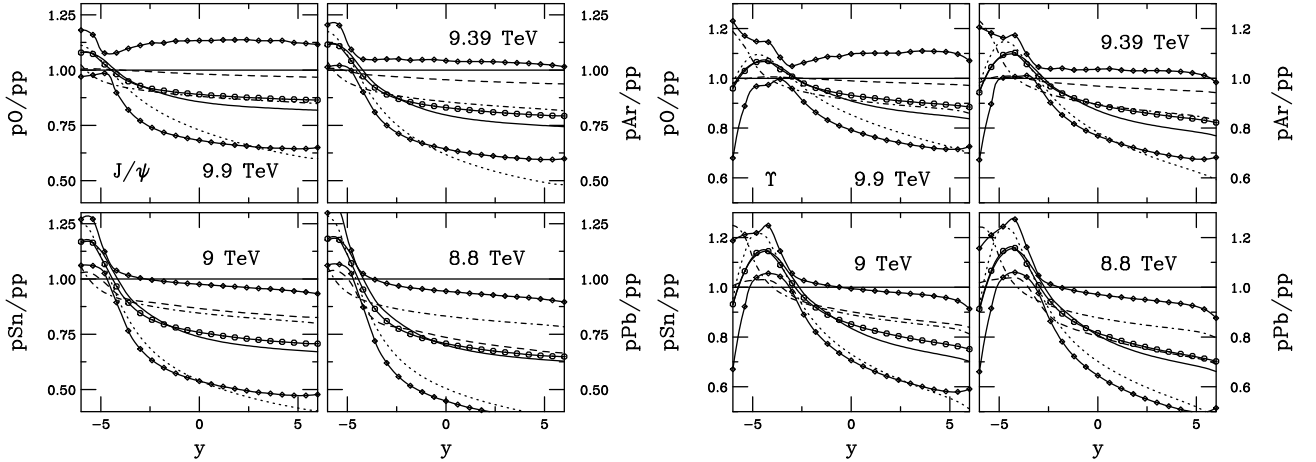


FIG. 4: The pA/pp ratios with both pA and pp collisions at the pA energy in the equal-speed frame. No rapidity shift has been taken into account. The effect of shadowing on J/ψ (left) and Υ (right) production is shown for pO at $\sqrt{s_{NN}} = 9.9$ TeV (upper left), pAr at $\sqrt{s_{NN}} = 9.39$ TeV (upper right), pSn at $\sqrt{s_{NN}} = 9$ TeV (lower left) and pPb at $\sqrt{s_{NN}} = 8.8$ TeV (lower right). The calculations are with CTEQ6 and employ the EKS98 (solid), nDSg (dashed), HKN (dot-dashed), EPS08 (dotted) and EPS09 (solid curves with smbols) shadowing parameterizations.

Rapidity dependence

The pA/pp ratios with equal pA and pp center-of-mass energies, shown in Figs. 4 and 5, illustrate the direct shadowing effect. The ratios are given both at the energy in the equal-speed frame, the likely $\sqrt{s_{NN}}$ for pA collisions (Fig. 4), and at the same $\sqrt{s_{NN}}$ as the corresponding AA collisions (Fig. 5). The results are shown for all shadowing parameterizations. The nuclear beam is assumed to be moving from positive to negative rapidity so that the smallest values of x probed in the nucleus are at large, positive y .

The LHC could be run as either a pA or an Ap collider. Since the ATLAS and CMS detectors are symmetric around $y = 0$ with central muon detectors in the range $|y| \leq 2.4$, ALICE is the only experiment that could benefit from running in both modes because the dimuon spectrometer covers $-4 < y < -2.4$ in these coordinates [40]. However, since ALICE has muon coverage in the largest y region, running in both modes could be an advantage for reconstructing the nuclear effects in quarkonium measurements, especially since the y distributions are rather flat over a broad rapidity range. The large rapidity rates are thus non-negligible.

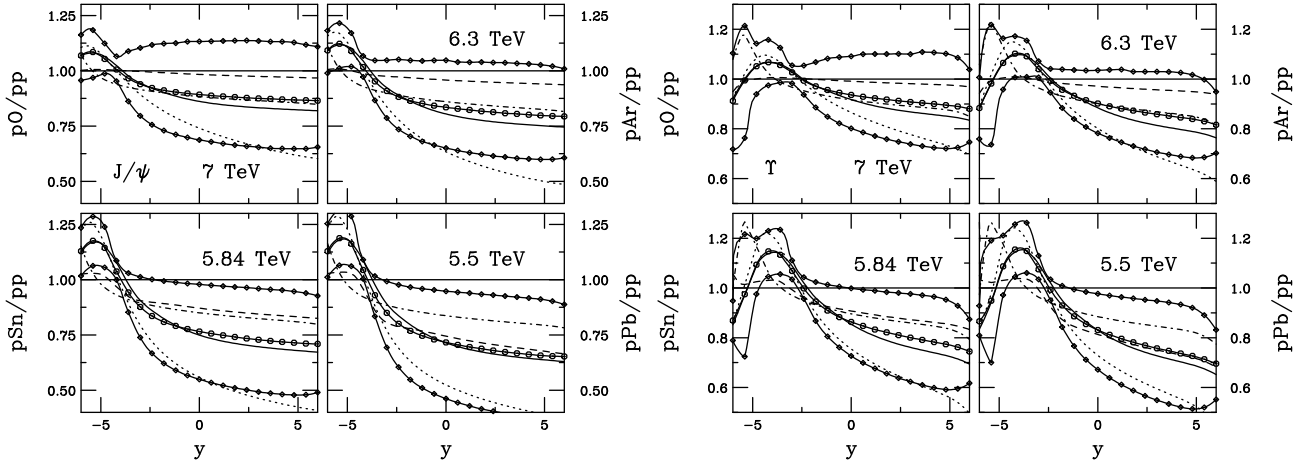


FIG. 5: The pA/pp ratios with both pA and pp collisions at the AA center-of-mass energy. The effect of shadowing on J/ψ (left) and Υ (right) production is shown for pO at $\sqrt{s_{NN}} = 7$ TeV (upper left), pAr at $\sqrt{s_{NN}} = 6.3$ TeV (upper right), pSn at $\sqrt{s_{NN}} = 6.14$ TeV (lower left) and pPb at $\sqrt{s_{NN}} = 5.5$ TeV (lower right). The calculations are with CTEQ6 and employ the EKS98 (solid), nDSg (dashed), HKN (dot-dashed), EPS08 (dotted) and EPS09 (solid curves with symbols) shadowing parameterizations.

The J/ψ ratios are shown on the left-hand side of the figures while the Υ results are on the right-hand side. Since shadowing is an initial-state effect, the same ratios would also be expected for the χ_c and ψ' on the left and the higher Υ states (Υ' , Υ'' , $\chi_b(1P)$ and $\chi_b(2P)$) on the right. The ratios in Figs. 4 and 5 are stretched mirror images of the gluon shadowing ratios in Fig. 3. The lowest x values are probed by the lightest nuclei since the center of mass energy is higher for nuclei with $Z/A \sim 0.5$ than heavier, neutron-rich nuclei with lower Z/A . The differences in the shadowing ratios for a given parameterization are greatest at large negative y where x is largest. As A increases and $\sqrt{s_{NN}}$ decreases, the antishadowing peak moves closer to midrapidity (less negative y). Increasing the scale from that appropriate for the J/ψ to that for the Υ also moves the antishadowing peak closer to $y = 0$. For example, the EKS98 and EPS08 antishadowing peaks are fully visible for Υ production, occurring at $y \sim -3.5$, while they only appear at $y \leq -5$ for the J/ψ . As μ^2 increases, the differences in the EPS09 sets becomes more pronounced at large x , leading to the more irregular shapes of the upper and lower limits of the EPS09 uncertainty range at negative rapidity. Note that the central ratio is smooth. Thus, the results in Figs. 4 and 5 suggest that by running the LHC in both pA and Ap modes the modification of the nuclear gluon parton density could be traced out over a wide x range, taking advantage of the ALICE muon coverage.

Finally, we note that at $y = 6$, corresponding to $x < 10^{-6}$, the EKS98 and nDSg shadowing ratios are outside their range of validity. This is also near the region where DGLAP evolution of the parton densities is likely to break down. Nonlinear evolution of the proton parton densities is expected at sufficiently small x . The onset of these nonlinearities is predicted to be at larger x for nuclei. However, it is not obvious that nonlinear parton evolution automatically leads to a *reduction* of the small x gluon density since it has to be taken in context with a re-evaluation of all the parton densities, not just the gluon density. See Ref. [41] for details of such modified parton densities and Refs. [42–44] for a discussion of the possible effect on charm production at the LHC.

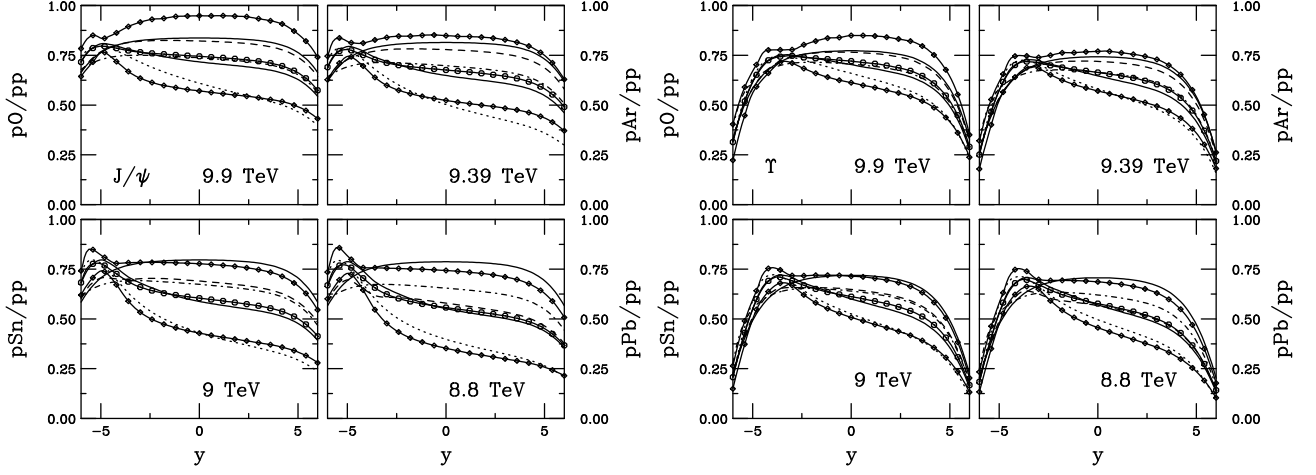


FIG. 6: The pA/pp ratios with the pp rapidity distributions calculated at $\sqrt{s} = 14$ TeV. While the pA distributions are calculated in the equal-speed frame, no rapidity shift has been taken into account. The effect of shadowing on J/ψ (left) and Υ (right) production is shown for pO at $\sqrt{s_{NN}} = 9.9$ TeV (upper left), pAr at $\sqrt{s_{NN}} = 9.39$ TeV (upper right), pSn at $\sqrt{s_{NN}} = 9$ TeV (lower left) and pPb at $\sqrt{s_{NN}} = 8.8$ TeV (lower right), all calculated in the equal-speed frame. The calculations are with CTEQ6 and employ the EKS98 (solid), nDSg (dashed), HKN (dot-dashed), EPS08 (dotted) and EPS09 (solid curves with symbols) shadowing parameterizations. The solid curve symmetric around $y = 0$ is the pA/pp ratio without shadowing.

Since it is more likely that the best pp reference data will be at $\sqrt{s} = 14$ TeV or 10 TeV for the initial LHC run, Figs. 6 and 7 show the pA/pp ratios with the pp reference at 14 TeV. The magnitude of the two ratios (for pA collisions in the equal-speed frame, Fig. 6, and at the same energy as the corresponding AA collisions, Fig. 7) is due to the difference in $\sqrt{s_{NN}}$ relative to 14 TeV. The pA ratios with the pA center-of-mass energies equal to those of AA collisions are lower. The rapidity distributions narrow while their magnitudes are reduced with decreasing $\sqrt{s_{NN}}$. Thus the pA/pp ratios without shadowing decrease steadily from 9.9 to 5.5 TeV while the narrowing of the ratios becomes more pronounced.

The symmetric solid curves in Figs. 6 and 7 are the pA/pp ratios without shadowing. Shadowing results in asymmetric ratios but since the pA phase space is narrower than that of 14 TeV pp collisions, the ratios in these figures turn over and drop to zero at large $|y|$. The narrower phase space has a bigger effect on the Υ production ratios since the full Υ rapidity range is within $|y| < 6$ while the J/ψ y distribution is broader. The antishadowing peak is lowered and broadened when dividing by the 14 TeV pp rapidity distribution and is only really apparent for the EKS98, EPS08 and EPS09 parameterizations. The EPS08 parameterization and the maximum shadowing allowed by EPS09 shows the most asymmetric curvature, especially for J/ψ . The EPS09 ratios suggest that the effect could be as large as obtained with EPS08 or small enough to be effectively indistinguishable from no shadowing. It will thus be harder to differentiate between shadowing parameterizations when employing the higher energy pp reference.

As discussed previously, there is an additional complication due to the rapidity shift of the pA center of rapidity in the equal-speed frame. The shift increases with A as Z/A decreases, reducing the energy of the ion beam relative to the proton beam. This results in nearly half a unit rapidity shift in pPb collisions, as shown in the center part of Table I, labeled pA . The pA/pp ratios including the rapidity shift and the maximum energy pp reference are shown in Fig. 8. Note that only the pA results in the equal-speed frame are shown. Since the proton beam momentum in pA collisions at the AA center-of-mass energy must be the same as that of the ion beam, $\Delta y_{cm}^{pA} = 0$. The pA rapidity distribution is given a positive shift, to the right, since the proton beam, at higher y , is assumed to come from the left and move to the right. Thus, at large negative y , the ratios are lower than in Figs. 6 and 7 and are flatter as a function of rapidity. While the nuclear effects on the parton densities are most difficult to disentangle here, this scenario is the most realistic. If the LHC is run with the proton and ion beam directions reversed, the antishadowing peak may be enhanced and the large positive rapidity ratios decreased.

The effect of the rapidity shift is reduced if dA collisions are run instead of pA collisions. The dA center-of-mass energy is closer to that of AA collisions since $Z/A < 1$ for the deuteron rather than equal to 1 as for protons. The ratios with the dA and pp collisions at the same center-of-mass energy per nucleon are shown in Fig. 9 (similar to Fig. 5 for pA). They are like those in Fig. 5 with equal pA and AA center-of-mass energies since $\sqrt{s_{NN}}$ is similar for dA and AA collisions. Shadowing effects on the deuteron are assumed to be negligible.

The results with a 14 TeV pp reference and the small rapidity shift taken in account, see Table I for Δy_{cm}^{dA} , are

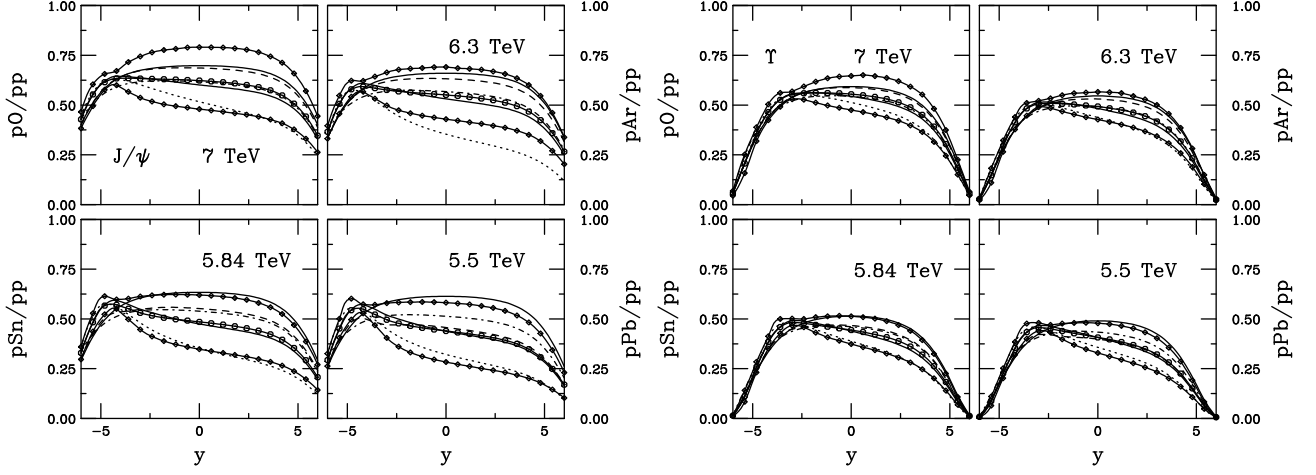


FIG. 7: The pA/pp ratios with the pp rapidity distributions calculated at $\sqrt{s} = 14$ TeV. The pp distributions are calculated at the AA center-of-mass energy. The effect of shadowing on J/ψ (left) and Υ (right) production is shown for pO at $\sqrt{s_{NN}} = 7$ TeV (upper left), pAr at $\sqrt{s_{NN}} = 6.3$ TeV (upper right), pSn at $\sqrt{s_{NN}} = 6.14$ TeV (lower left) and pPb at $\sqrt{s_{NN}} = 5.5$ TeV (lower right). The ratios are calculated at the AA energy. The calculations are with CTEQ6 and employ the EKS98 (solid), nDSg (dashed), HKN (dot-dashed), EPS08 (dotted) and EPS09 (solid curves with symbols) shadowing parameterizations. The solid curve symmetric around $y = 0$ is the pA/pp ratio without shadowing.

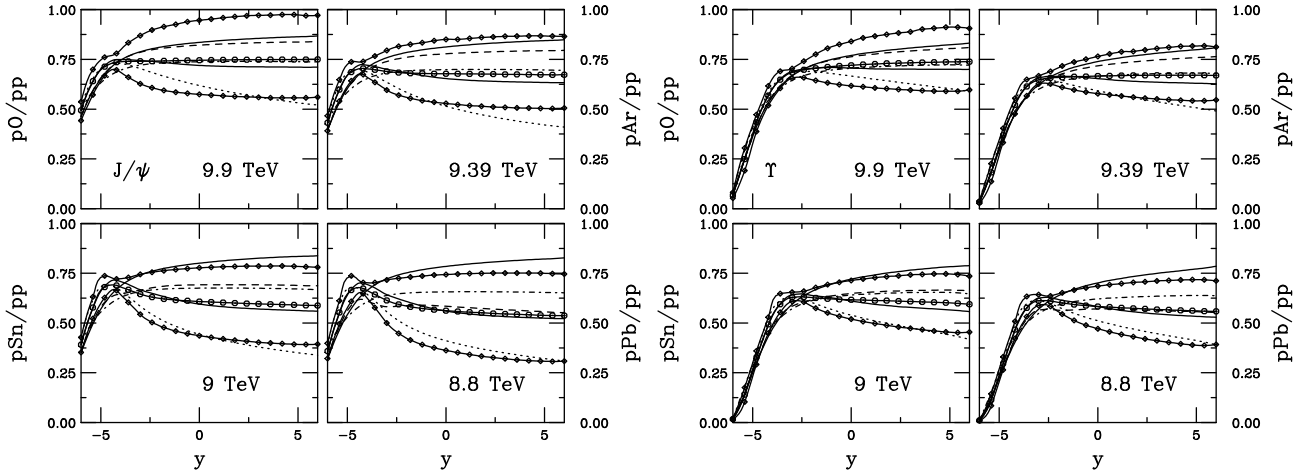


FIG. 8: The pA/pp ratios with the pp rapidity distributions calculated at $\sqrt{s} = 14$ TeV. The pA rapidity distributions are calculated in the equal-speed frame with the rapidity shift taken into account. The effect of shadowing on J/ψ (left) and Υ (right) production is shown for pO at $\sqrt{s_{NN}} = 9.9$ TeV (upper left), pAr at $\sqrt{s_{NN}} = 9.39$ TeV (upper right), pSn at $\sqrt{s_{NN}} = 9$ TeV (lower left) and pPb at $\sqrt{s_{NN}} = 8.8$ TeV (lower right). The calculations are with CTEQ6 and employ the EKS98 (solid), nDSg (dashed), HKN (dot-dashed), EPS08 (dotted) and EPS09 (solid curves with symbols) shadowing parameterizations. The upper solid curve at $y > 0$ is the shifted pA/pp ratio without shadowing.

shown in Fig. 10. Recall that there is no rapidity shift for dO collisions since $Z_d/A_d = Z_O/A_O = 0.5$. Thus the equal-speed and center-of-rapidity frames coincide. In dPb collisions, since $\Delta y_{cm}^{dA} < 0.06$, the shift is negligible. Thus the dA rapidity distributions relative to the 14 TeV pp reference *with* the rapidity shift, shown in Fig. 10, are similar to those in Fig. 7 with $\Delta y_{cm}^{pA} = 0$ and the same $\sqrt{s_{NN}}$ in pA and AA collisions. Note, however, that the ratios in Fig. 10 are somewhat closer to unity since the dA center-of-mass energy is larger. Thus the more realistic dA scenario shown in Fig. 10 would be preferable for determining nuclear effects on the parton densities both because of the relatively similar center-of-mass energies and the smaller rapidity shift.

We now extrapolate to AA interactions to show the projected CNM effects from shadowing alone. The results for AA collisions are shown in Figs. 11 and 12. The AA/ pp ratio with both systems calculated at the AA center-of-mass energy are shown in Fig. 11 while the 14 TeV pp reference is employed to obtain the ratios in Fig. 12. The results in

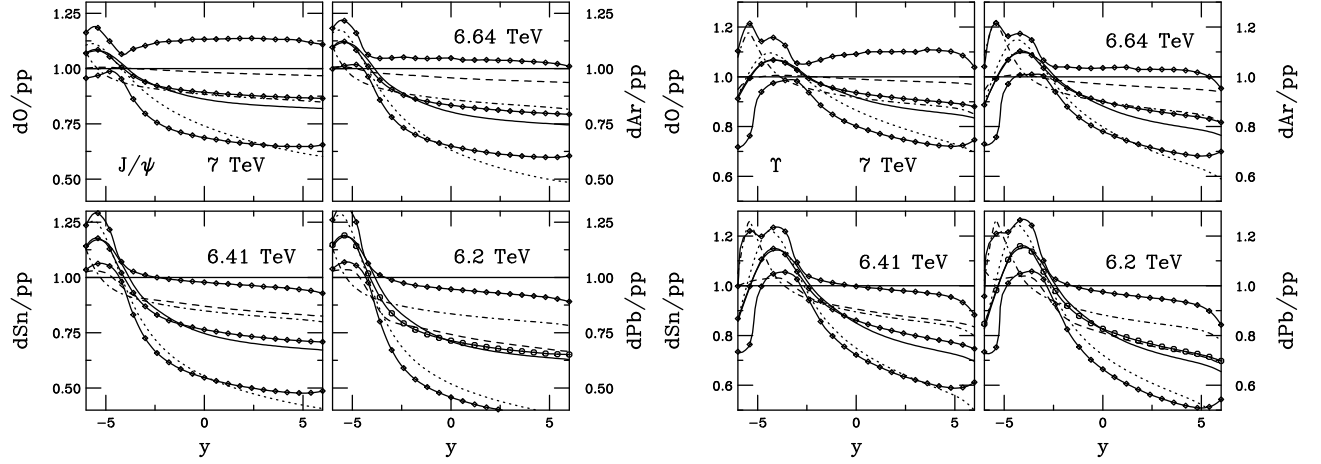


FIG. 9: The dA/pp ratios with both dA and pp collisions at the dA energy in the equal-speed frame. No rapidity shift has been taken into account. The effect of shadowing on J/ψ (left) and Υ (right) production is shown for dO at $\sqrt{s_{NN}} = 7$ TeV (upper left), dAr at $\sqrt{s_{NN}} = 6.64$ TeV (upper right), dSn at $\sqrt{s_{NN}} = 6.41$ TeV (lower left) and dPb at $\sqrt{s_{NN}} = 6.2$ TeV (lower right). The calculations are with CTEQ6 and employ the EKS98 (solid), nDSg (dashed), HKN (dot-dashed), EPS08 (dotted) and EPS09 (solid curves with symbols) shadowing parameterizations.

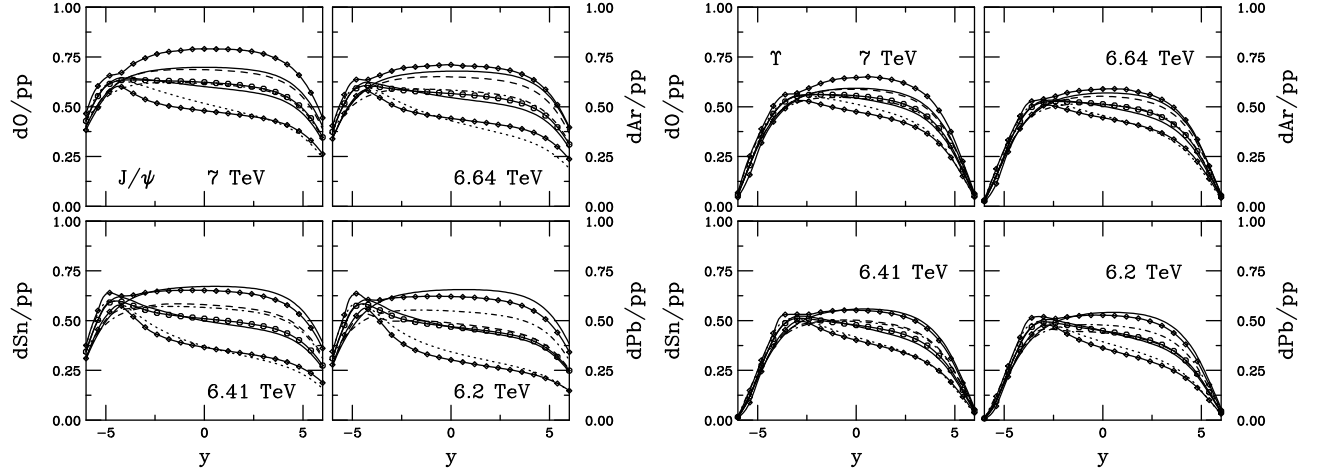


FIG. 10: The dA/pp ratios with the pp distributions calculated at $\sqrt{s} = 14$ TeV and the dA rapidity shift taken into account. The effect of shadowing on J/ψ (left) and Υ (right) production is shown for dO at $\sqrt{s_{NN}} = 7$ TeV (upper left), dAr at $\sqrt{s_{NN}} = 6.64$ TeV (upper right), dSn at $\sqrt{s_{NN}} = 6.41$ TeV (lower left) and dPb at $\sqrt{s_{NN}} = 6.2$ TeV (lower right). The calculations are with CTEQ6 and employ the EKS98 (solid), nDSg (dashed), HKN (dot-dashed), EPS08 (dotted) and EPS09 (solid curves with symbols) shadowing parameterizations. The symmetric solid curve is the result without shadowing.

Fig. 11 are essentially the convolutions of the pA/pp ratios (with the same $\sqrt{s_{NN}}$ for both systems and no rapidity shift) shown in Fig. 5 with their mirror image Ap/pp ratios. While the AA ratios exhibit antishadowing peaks at $y \sim \pm(4-5)$, the AA/pp ratios are less than unity everywhere because the product of the pA/pp ratios at positive y and the Ap/pp ratios at negative y is always smaller than one, *e.g.* $pA/pp(y \sim 5) \sim 0.6-0.75$ while $Ap/pp(y \sim -5) \sim 1.2$. Thus, when all ratios are calculated at the AA center-of-mass energy, assuming factorization of AA collisions into a convolution of pA and Ap collisions,

$$\frac{AA}{pp}(y \sim \pm 5) = \frac{pA}{pp}(y \sim 5) \times \frac{Ap}{pp}(y \sim -5) < 1. \quad (13)$$

Gluon saturation models predict that factorization is inapplicable due to the coherence of the interaction [45].

As is the case for the RHIC AA calculations at $\sqrt{s_{NN}} = 200$ GeV [46], there is typically more suppression predicted at $y = 0$ than at more forward and backward rapidities for all the shadowing parameterizations as well as for both J/ψ and Υ production. At RHIC, the AA data are more suppressed at forward rapidity than at central rapidity,

both in the minimum bias data as a function of rapidity and as a function of collision centrality, as quantified by the number of participant nucleons. Standard models of shadowing alone or shadowing with absorption by nucleons in cold nuclear matter or shadowing combined with dissociation in a quark-gluon plasma leads to strong suppression at central rapidities. However, J/ψ regeneration by coalescence of c and \bar{c} quarks in the medium [13, 47] is biased toward central rapidities and could lead to more suppression at forward rapidity relative to central rapidity since the rapidity distribution of J/ψ production by coalescence is expected to be narrower than the initial J/ψ rapidity distribution [47]. Thus, with coalescence, there should be more suppression at forward y than at midrapidity. The same trend should hold at the LHC. Coalescence production of the J/ψ should be even more important than at RHIC since more $c\bar{c}$ pairs are created in a central Pb+Pb collision at $\sqrt{s_{NN}} = 5.5$ TeV. We can also expect that Υ production by coalescence may be similar to that expected for the J/ψ at RHIC since the $b\bar{b}$ production cross section at the LHC will be similar to the $c\bar{c}$ production cross section at RHIC [14].

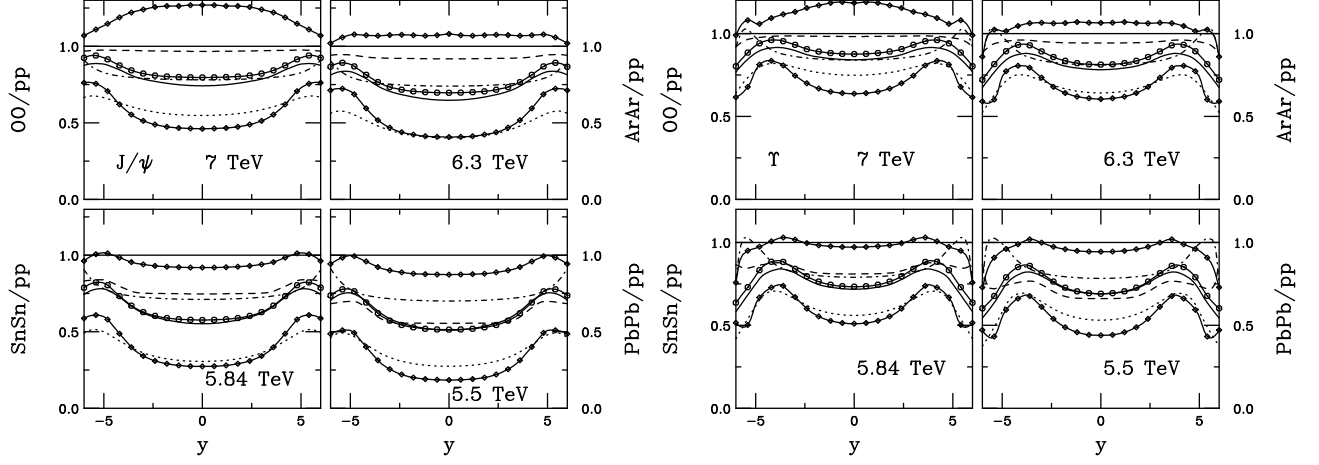


FIG. 11: The AA/pp ratios with both AA and pp collisions calculated at the AA center-of-mass energy. The effect of shadowing on J/ψ (left) and Υ (right) production is shown for O+O at $\sqrt{s_{NN}} = 7$ TeV (upper left), Ar+Ar at $\sqrt{s_{NN}} = 6.3$ TeV (upper right), Sn+Sn at $\sqrt{s_{NN}} = 6.14$ TeV (lower left) and Pb+Pb at $\sqrt{s_{NN}} = 5.5$ TeV (lower right). The calculations are with CTEQ6 and employ the EKS98 (solid), nDSg (dashed), HKN (dot-dashed), EPS08 (dotted) and EPS09 (solid curves with symbols) shadowing parameterizations.

The AA/pp ratios with the 14 TeV pp reference, shown in Fig. 12, are relatively flat. The dip around midrapidity has been washed out, except for the J/ψ ratios calculated with the EKS98, EPS08, and EPS09 (central and maximum shadowing) parameterizations where some indication remains. For comparison, the AA/pp ratios without shadowing are shown in the upper solid curves.

Impact parameter dependence

We now discuss the impact parameter dependence of quarkonium production at the LHC. Unfortunately, there is little relevant data on the spatial dependence of shadowing. Fermilab experiment E745 studied the spatial distribution of nuclear structure functions with νN interactions in emulsion. The presence of one or more dark tracks from slow protons is used to infer a more central interaction [48]. For events with no dark tracks, no shadowing is observed while, for events with dark tracks, shadowing is enhanced over spatially-independent measurements from other experiments. Unfortunately, this data is too limited to be used in a fit of the spatial dependence.

The minimum bias shadowing we have discussed up to now is homogeneous, impact parameter-integrated shadowing. The impact parameter-dependent results shown in this section portray inhomogeneous shadowing. In central collisions, with small impact parameter, b , we can expect inhomogeneous shadowing to be stronger than the homogeneous result. In peripheral (large impact parameter) collisions, inhomogeneous effects are weaker than the homogeneous results but some shadowing is still present due to the overlapping tails of the density distributions. The stronger the homogeneous shadowing, the larger the difference between the central and peripheral results.

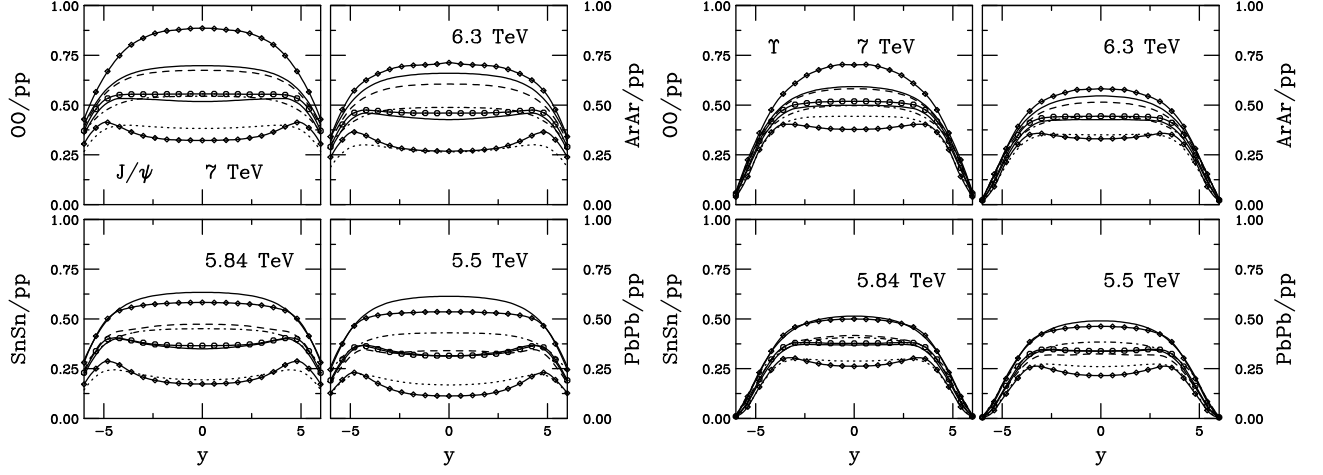


FIG. 12: The AA/pp ratios with the pp rapidity distributions calculated at $\sqrt{s} = 14$ TeV. The effect of shadowing on J/ψ (left) and Υ (right) production is shown for O+O at $\sqrt{s_{NN}} = 7$ TeV (upper left), Ar+Ar at $\sqrt{s_{NN}} = 6.3$ TeV (upper right), Sn+Sn at $\sqrt{s_{NN}} = 6.14$ TeV (lower left) and Pb+Pb at $\sqrt{s_{NN}} = 5.5$ TeV (lower right). The calculations are with CTEQ6 and employ the EKS98 (solid), nDSg (dashed), HKN (dot-dashed), EPS08 (dotted) and EPS09 (solid curves with symbols) shadowing parameterizations. The upper solid curve is the AA/pp ratio without shadowing.

We assume that the shadowing is proportional to the parton path through the nucleus [49],

$$S_{p,\rho}^i(A, x, Q^2, \vec{r}, z) = 1 + N_\rho(S_p^i(A, x, Q^2) - 1) \frac{\int dz \rho_A(\vec{r}, z)}{\int dz \rho_A(0, z)}, \quad (14)$$

where N_ρ is chosen to satisfy the normalization condition in Eq. (5). The integral over z in Eq. (14) includes the material traversed by the incident nucleon. At large distances, $s \gg R_A$, the nucleons behave as free particles, while in the center of the nucleus, the modifications are larger than the average value S_p^i .

We calculate the nuclear suppression factor, R_{AB} , for pA , dA and AA collisions. The suppression factor is defined as the ratio [50]

$$R_{AB}(N_{\text{part}}; b) = \frac{d\sigma_{AB}/dy}{T_{AB}(b)d\sigma_{pp}/dy} \quad (15)$$

where $d\sigma_{AB}/dy$ and $d\sigma_{pp}/dy$ are the quarkonium rapidity distributions in AB and pp collisions and T_{AB} is the nuclear overlap function,

$$T_{AB}(b) = \int d^2s dz dz' \rho_A(s, z) \rho_B(|\vec{b} - \vec{s}|, z'). \quad (16)$$

In pA collisions, we assume that the proton has a negligible size, $\rho_A(s, z) = \delta(s)\delta(z)$ so that $T_{AB}(b)$ collapses to the nuclear profile function $T_B(b) = \int dz' \rho_B(b, z')$. The deuteron cannot be treated like a point particle since it is large and diffuse. We use the Hülthen wave function [51] to calculate the deuteron density distribution. However, we do not include shadowing effects on the deuteron.

We show the pA and dA suppression factors as a function of impact parameter in Figs. 13 and 14 respectively. We concentrate on the largest A ion, Pb, to maximize the relevant impact parameter range. The results in Fig. 13 are given for three values of rapidity: $y = -4$ (backward rapidity, in the antishadowing region for Υ), $y = 0$ (midrapidity) and $y = 4$ (forward rapidity, where fairly strong shadowing is expected). We present J/ψ ratios on top and Υ ratios on the bottom. For comparison, the horizontal lines, centered around the average path length through the lead nucleus, $b \sim (3/4)R_{\text{Pb}}$, show the impact parameter-integrated ratios in Fig. 4. The b dependence is strong, resulting in $R_{p\text{Pb}} \sim 1$ for $b > R_{\text{Pb}}$. Shadowing is stronger in central collisions than the average integrated value, as expected. Because the average decreases at forward rapidities while the spatial dependence is relatively unchanged, the strongest b dependence is seen for the most forward rapidity value, $y = 4$. The nDSg, EKS98, and EPS09 shadowing ratios in Fig. 3 are very similar for lead nuclei, thus their suppression ratios are also similar. Since only one nuclear density profile is involved in the calculation of R_{pA} , the impact parameter dependence reflects that of Eq. 14 rather directly.

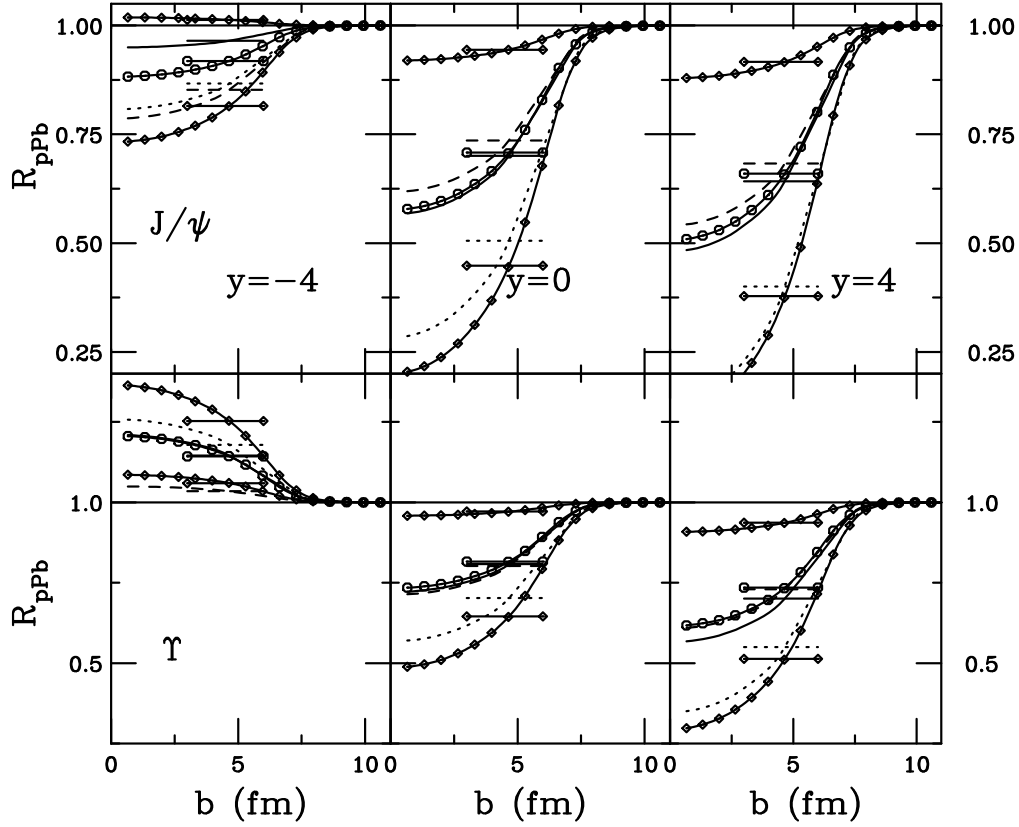


FIG. 13: The suppression factor R_{pPb} at $y = -4$ (left), 0 (center) and 4 (right) as a function of b . The result is shown for J/ψ (top) and Υ (bottom) in $p+Pb$ relative to pp collisions at the same energy, $\sqrt{s_{NN}} = 8.8$ TeV, and employ the EKS98 (solid), nDSg (dashed), EPS08 (dotted) and EPS09 (solid curves with symbols) shadowing parameterizations. The horizontal lines show the impact-parameter integrated results.

A weaker impact parameter dependence is seen for d+Pb collisions in Fig. 14. The overall shadowing effect is reduced since the energy is lower, $\sqrt{s_{NN}} = 6.2$ TeV relative to 8.8 TeV for pPb collisions. In addition, shadowing persists to large values of impact parameter. In a heavy nucleus, the density is large and approximately constant except close to the surface, as expressed by the Woods-Saxon density distributions [16]. However, the diffuse wavefunction of the deuteron has a finite amplitude at surprisingly large distances. These long tails produce some remnant shadowing effect even at very large b , as seen in Fig. 14. See also the discussion in Ref. [49].

The d+Au results at RHIC have been presented as a function of the number of binary nucleon-nucleon collisions, $N_{coll}(s_{NN}; b) = \sigma_{inel}(s_{NN})T_{AB}(b)$, rather than impact parameter itself, see Ref. [38] for details. The number of collisions is greatest for the most central collisions, $b \approx 0$, and decreases with increasing b . Since the inelastic nucleon-nucleon cross section, $\sigma_{inel}(s_{NN})$, is energy dependent, the number of collisions increases with energy even though $T_{AB}(b)$ does not. Thus $N_{coll}(s_{NN}; b)$ is significantly larger at the LHC than at RHIC for the same AB system because of the considerable increase in $\sigma_{inel}(s_{NN})$ (from 42 mb at $\sqrt{s_{NN}} = 200$ GeV to 75 mb in Pb+Pb collisions at $\sqrt{s_{NN}} = 5.5$ TeV).

The results for nucleus-nucleus collisions are presented as a function of the number of participant nucleons, N_{part} , which depends on b as

$$N_{part}(b) = \int d^2s \left[T_A(s)(1 - \exp[-\sigma_{inel}T_B(|\vec{b} - \vec{s}|)]) + T_B(|\vec{b} - \vec{s}|)(1 - \exp[-\sigma_{inel}T_A(s)]) \right]. \quad (17)$$

Large values of N_{part} are obtained for small impact parameters with $N_{part}(b = 0) = 2A$ for spherical nuclei. Small values of N_{part} occur in very peripheral collisions. Figure 15 shows $R_{AA}(N_{part})$, at $y = 0$ for the four AA systems and energies of Fig. 11 where the pp rapidity distribution is calculated at the same center-of-mass energy as the AA distribution. A similar pattern is observed for other values of y since the AA/pp ratios are approximately independent

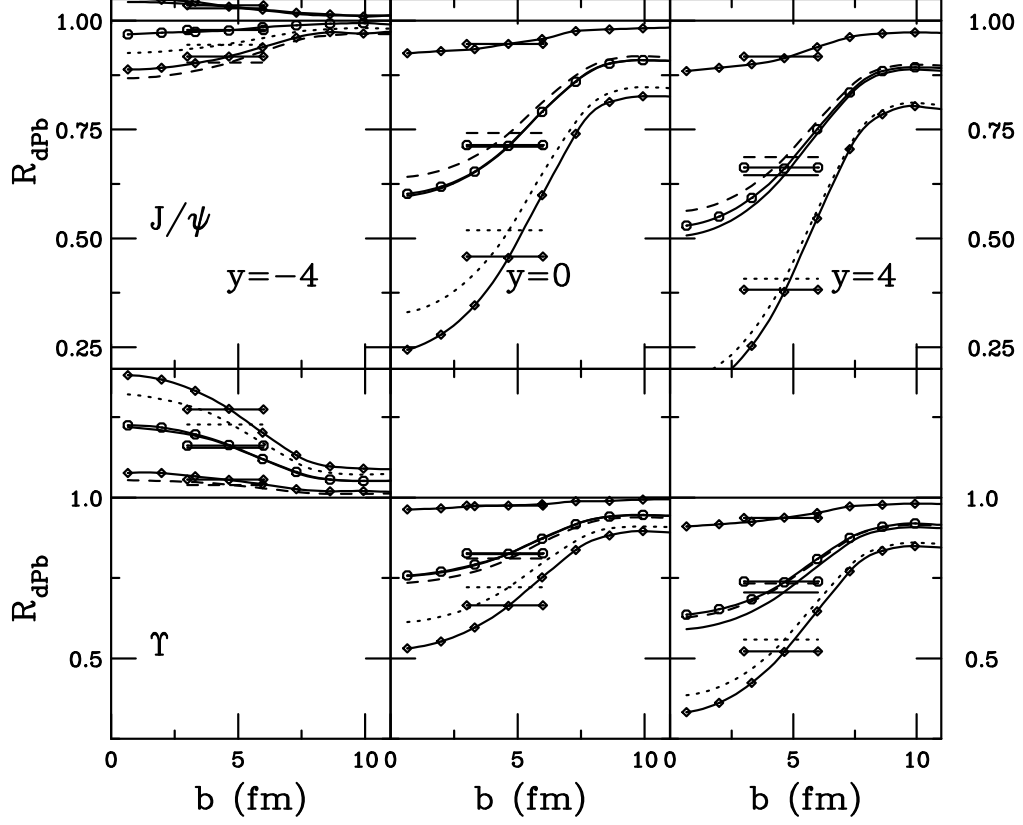


FIG. 14: The suppression factor R_{dPb} at $y = -4$ (left), 0 (center) and 4 (right) as a function of b . The result is shown for J/ψ (top) and Υ (bottom) in d+Pb relative to pp collisions at the same energy, $\sqrt{s_{NN}} = 6.2$ TeV, and employ the EKS98 (solid), nDSg (dashed), EPS08 (dotted) and EPS09 (solid curves with symbols) shadowing parameterizations. The horizontal lines show the impact-parameter integrated results.

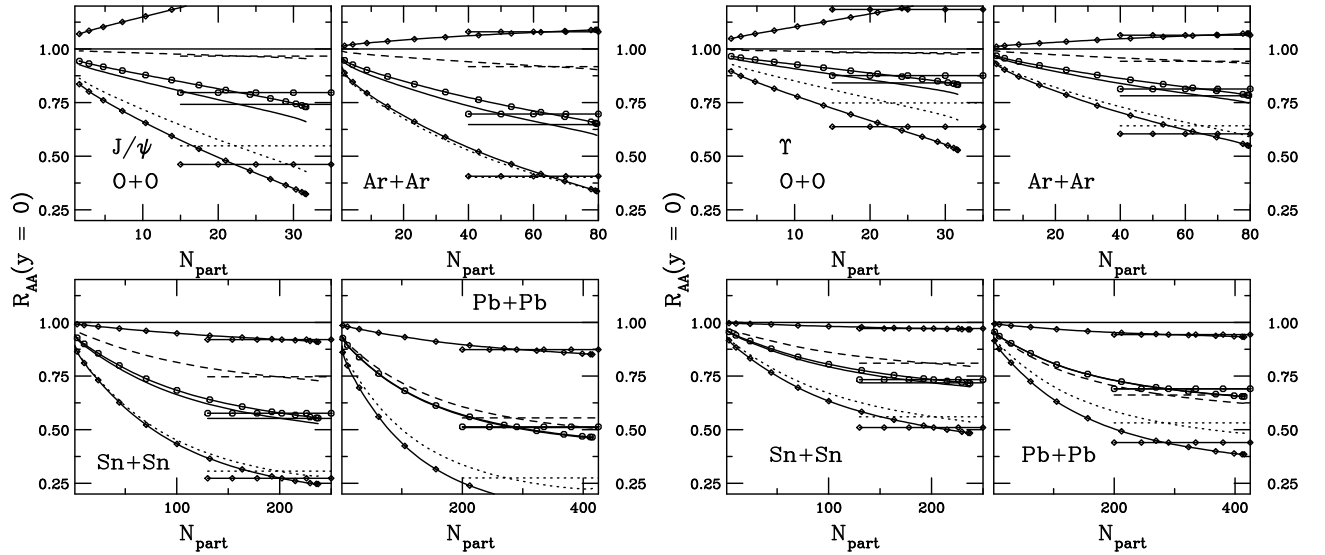


FIG. 15: The suppression factor R_{AA} at $y = 0$ as a function of N_{part} . The effect of shadowing on J/ψ (left) and Υ (right) production is shown for O+O at $\sqrt{s_{NN}} = 7$ TeV (upper left), Ar+Ar at $\sqrt{s_{NN}} = 6.3$ TeV (upper right), Sn+Sn at $\sqrt{s_{NN}} = 6.14$ TeV (lower left) and Pb+Pb at $\sqrt{s_{NN}} = 5.5$ TeV (lower right). The calculations are with CTEQ6 and employ the EKS98 (solid), nDSg (dashed), EPS08 (dotted) and EPS09 (solid curves with symbols) shadowing parameterizations.

of rapidity over a rather broad range. The AA/pp ratio at $y = 0$ from Fig. 11 is indicated by a horizontal line. Note that $R_{AA}(N_{\text{part}})$ in Fig. 15 is equal to AA/pp in Fig. 11 for $N_{\text{part}}(b \approx R_A)$. In small systems, $R_{AA}(N_{\text{part}})$ is almost linear with more curvature appearing for larger collision systems.

Since the pp reference is not likely to be immediately available at the AA center-of-mass energy, it is preferable to study ratios of two quantities measured at the same energy. In this case, the ratio of AB cross sections in central relative to peripheral collisions,

$$R_{CP}(y) = \frac{T_{AB}(b_P)}{T_{AB}(b_C)} \frac{d\sigma_{AB}(b_C)/dy}{d\sigma_{AB}(b_P)/dy}, \quad (18)$$

where b_C and b_P correspond to central and peripheral values of the impact parameter, is determined. Indeed, shadowing may best be probed by R_{CP} measurements in asymmetric systems since the most peripheral collisions are a good approximation to nucleon-nucleon collisions. The same rapidity shift is common to both central and peripheral collisions.

In fact, studying R_{CP} in pA and dA collisions could provide a direct measure of shadowing if absorption is negligible since higher-order corrections unrelated to shadowing cancel in the ratio [49]. As an example of an asymmetric system, Fig. 16 presents $R_{CP}(y)$ for $d+Pb$ collisions with $b_C = 0$ and $b_P = R_A$. As expected, the resulting $R_{CP}(y)$ are very similar to the impact-parameter averaged dA/pp ratios shown in Fig. 9. Since $R_{CP}(y)$ with $b_P = 2R_A$ are similar to those in Fig. 16, they are not shown.

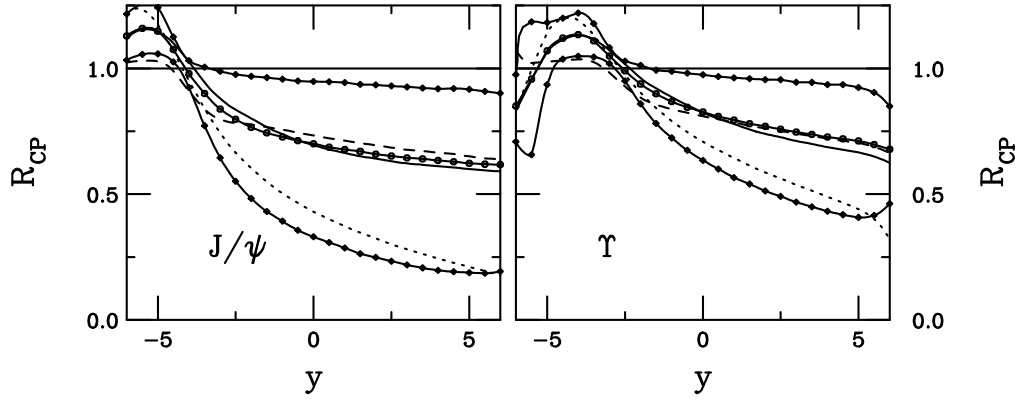


FIG. 16: The central-to-peripheral ratios, R_{CP} , as a function of rapidity for $b = R_A$ relative to $b = 0$ for $d+Pb$ collisions at $\sqrt{s_{NN}} = 6.2$ TeV. The calculations are with CTEQ6 and employ the EKS98 (solid), nDSg (dashed), EPS08 (dotted) and EPS09 (solid curves with symbols) shadowing parameterizations.

Figures 17 and 18 show the values of R_{CP} for $b_P = R_A$ and $2R_A$ relative to $b_C = 0$ in the four AA systems studied for the J/ψ (Fig. 17) and the Υ (Fig. 18). Since the change in $R_{AA}(N_{\text{part}})$ between $b_C = 0$ and $b_P = R_A$ is small (see Fig. 15), these ratios are almost independent of rapidity and give R_{CP} close to unity. On the other hand, the weaker shadowing effect at $b_P = 2R_A$ produces a stronger rapidity dependence and a lower R_{CP} . Note that, as in Fig. 16, $R_{CP}(y)$ for $b_P \approx 2R_A$ is similar to $AA/pp(y > 0)$ in Fig. 11. Thus, if no other medium effects are present, it is possible to trace the shadowing effect rather accurately by determining R_{CP} for sufficiently narrow centrality bins.

SUMMARY

We have provided a survey of the quarkonium total cross sections to next-to-leading order in the color evaporation model for all AB combinations and energies at the LHC. We have included initial-state shadowing, employing several parameterizations of the nuclear modifications of the parton densities.

We have calculated pA/pp and dA/pp ratios from the most naive (both systems at the same energy) to the most realistic (the pp reference at 14 TeV and the rapidity shift of pA interactions in the equal-speed frame). The most

² We do not show R_{CP} for pA collisions because centrality is harder to define.

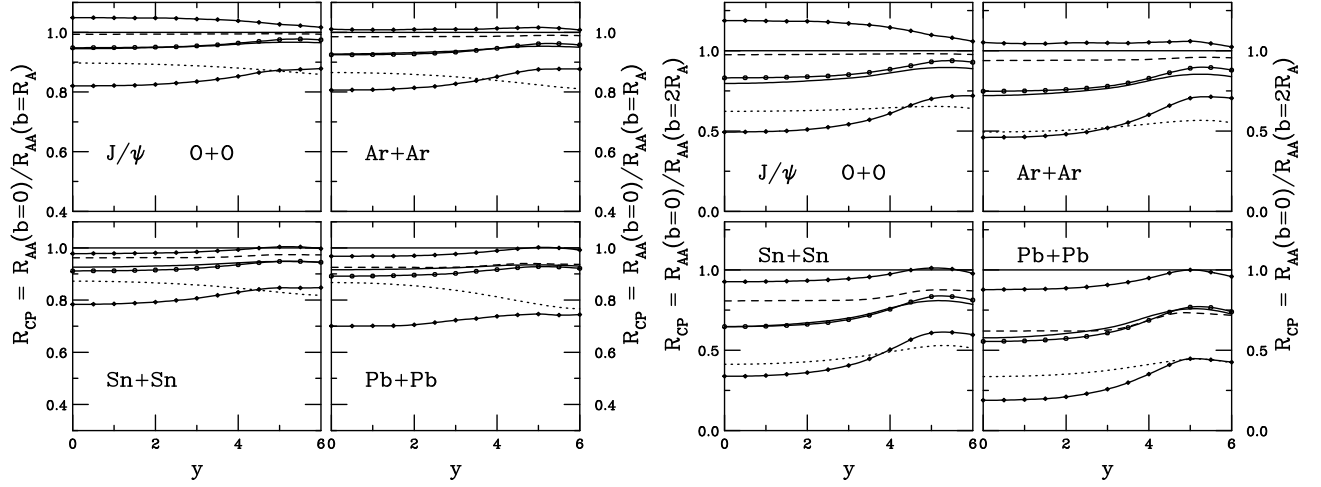


FIG. 17: The central-to-peripheral ratios, $R_{CP}(y)$, for $b = R_A$ (left) and $b = 2R_A$ (right) relative to $b = 0$. The effect of shadowing on J/ψ production is shown for O+O at $\sqrt{s_{NN}} = 7$ TeV (upper left), Ar+Ar at $\sqrt{s_{NN}} = 6.3$ TeV (upper right), Sn+Sn at $\sqrt{s_{NN}} = 6.14$ TeV (lower left) and Pb+Pb at $\sqrt{s_{NN}} = 5.5$ TeV (lower right). The calculations are with CTEQ6 and employ the EKS98 (solid), nDSg (dashed), EPS08 (dotted), and EPS09 (solid curves with symbols) shadowing parameterizations.

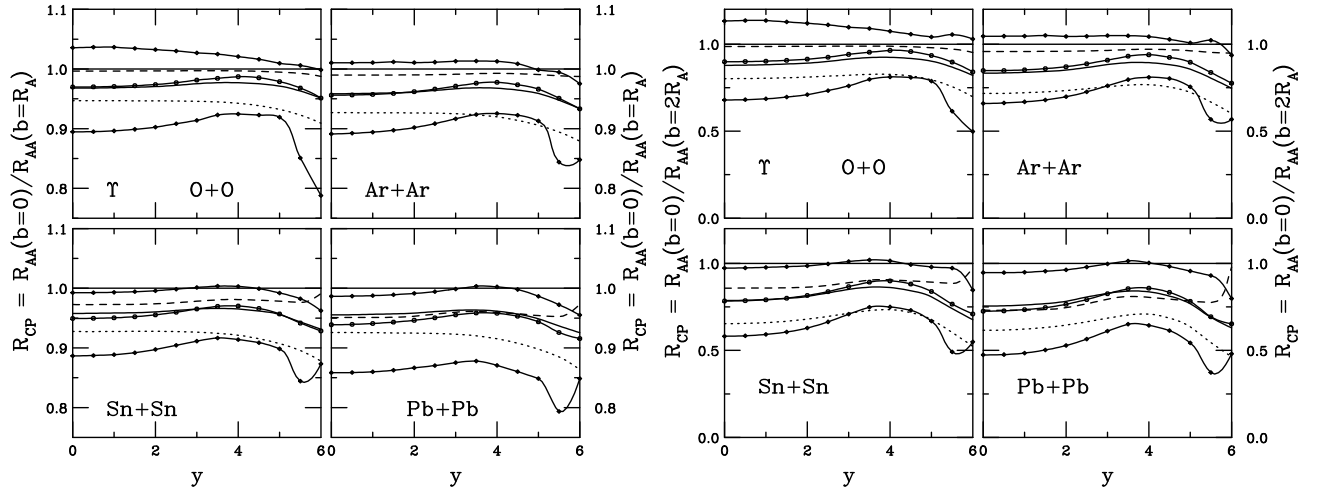


FIG. 18: The central-to-peripheral ratios, $R_{CP}(y)$, for $b = R_A$ (left) and $b = 2R_A$ (right) relative to $b = 0$. The effect of shadowing on Υ production is shown for O+O at $\sqrt{s_{NN}} = 7$ TeV (upper left), Ar+Ar at $\sqrt{s_{NN}} = 6.3$ TeV (upper right), Sn+Sn at $\sqrt{s_{NN}} = 6.14$ TeV (lower left) and Pb+Pb at $\sqrt{s_{NN}} = 5.5$ TeV (lower right). The calculations are with CTEQ6 and employ the EKS98 (solid), nDSg (dashed), EPS08 (dotted), and EPS09 (solid curves with symbols) shadowing parameterizations.

naive ratios are most straightforward for extracting the nuclear gluon distributions. It is still possible to use the most realistic ratios but more work is needed. The AA studies require good understanding of the nuclear gluon distribution to extract hot and dense matter effects. The dA/pp calculations are likely to be most useful since the dA center-of-mass energy is closer to the AA energy and has a smaller rapidity shift than pA collisions in the equal-speed frame.

To more cleanly extract the parton densities at LHC energies, it would be preferable to have ep and eA data at the appropriate x and Q^2 range of the LHC data. (The HERA x range reaches to approximately the value appropriate for J/ψ production in 5.5 TeV/nucleon collisions at midrapidity. Unfortunately, the Q^2 probed at these x values is smaller than the J/ψ mass scale.) So far, the nDIS data is not available at small enough x values and, simultaneously, large enough Q^2 to be relevant for quarkonium production at high energies. While electron-proton collisions, as studied at HERA, would be useful for obtaining the baseline in pp, it is not sufficient for pA.

The shadowing parameterizations used in our study exhibit a wide range of behavior for the nuclear gluon density at

low x , outside the current range of the fits from fixed target data at higher x and low Q^2 . If nuclear data were available from eA collisions, the nuclear gluon densities could be more precisely pinned down by global analyses. However, even in nDIS the nuclear gluon density is not directly probed but can only be studied via the scale dependence of the nuclear structure function. If the nuclear absorption of quarkonium production can indeed be ignored at LHC energies, it may be possible to use the different scales of J/ψ and Υ production to study the scale dependence of the gluon density in the nucleus as well as in the proton. We note that, since we have assumed absorption is negligible at the LHC and include no other cold nuclear matter effect, the uncertainties on the ratios can be obtained from the EPS09 bands shown in the figures. However, if other effects are included a more extensive error analysis, including the uncertainties on other effects, is necessary.

Finally, we note that the central-to-peripheral ratio, R_{CP} , may be useful for extracting the shadowing effect at a given collision energy if the impact parameter bins are narrow enough. This ratio is advantageous because it can be made at the same collision energy with the same rapidity shift.

Acknowledgements

We thank K. J. Eskola, H. Paukkunen and C. Salgado for providing the EPS09 files and for discussions. This work was performed under the auspices of the U.S. Department of Energy by Lawrence Livermore National Laboratory under Contract DE-AC52-07NA27344 and was also supported in part by the National Science Foundation Grant NSF PHY-0555660.

-
- [1] I. Arsene *et al.* (BRAHMS Collaboration), Phys. Rev. Lett. **93**, 242303 (2004) [arXiv:nucl-ex/0403005].
 - [2] K. J. Eskola, H. Paukkunen and C. A. Salgado, JHEP **0807**, 102 (2008) [arXiv:0802.0139 [hep-ph]].
 - [3] S. S. Adler *et al.* (PHENIX Collaboration), Phys. Rev. Lett. **98**, 172302 (2007) [arXiv:nucl-ex/0610036].
 - [4] K. J. Eskola, H. Paukkunen and C. A. Salgado, JHEP **0904**, 065 (2009) [arXiv:0902.4154 [hep-ph]].
 - [5] R. Baier and R. Rückl, Z. Phys. C **19**, 251 (1983); G. A. Schuler, CERN Preprint, CERN-TH.7170/94.
 - [6] F. Abe *et al.* (CDF Collaboration), Phys. Rev. Lett. **79**, 572 (1997); *ibid*, 578.
 - [7] M. Klasen, Rev. Mod. Phys. **74**, 1221 (2002) [arXiv:hep-ph/0206169].
 - [8] J.-P. Lansberg, Int. J. Mod. Phys. A **21**, 3857 (2006) [arXiv:hep-ph/0602091]; H. Haberzettl and J.-P. Lansberg, Phys. Rev. Lett. **100**, 032006 (2008) [arXiv:0709.3471 [hep-ph]].
 - [9] E. G. Ferreira, F. Fleuret, J.-P. Lansberg and A. Rakotozafindrabe, arXiv:0809.4684 [hep-ph].
 - [10] G. T. Bodwin, E. Braaten and G. P. Lepage, Phys. Rev. D **1**, 1125 (1995); **55**, 5853(E) (1997) [arXiv:hep-ph/9407339].
 - [11] T. Affolder *et al.* (CDF Collaboration), Phys. Rev. Lett. **85**, 2886 (2000) [arXiv:hep-ex/0004027]; A. Abulencia *et al.* (CDF Collaboration), Phys. Rev. Lett. **99**, 132001 (2007) [arXiv:0704.0638 [hep-ex]].
 - [12] R. Gavai, D. Kharzeev, H. Satz, G. A. Schuler, K. Sridhar and R. Vogt, Int. J. Mod. Phys. A **10**, 3043 (1995) [arXiv:hep-ph/9502270].
 - [13] M. Bedjidian *et al.*, arXiv:hep-ph/0311048.
 - [14] A. D. Frawley, T. Ullrich and R. Vogt, Phys. Rept. **462**, 125 (2008) [arXiv:0806.1013 [nucl-ex]].
 - [15] M. L. Mangano, P. Nason, and G. Ridolfi, Nucl. Phys. B **373**, 295 (1992).
 - [16] C. W. deJager, H. deVries and C. deVries, Atomic Data and Nuclear Data Tables **14**, 485 (1974).
 - [17] M. J. Leitch *et al.* (E866 Collaboration), Phys. Rev. Lett. **84**, 3256 (2000) [arXiv:nucl-ex/9909007].
 - [18] D. M. Alde *et al.* (E772 Collaboration), Phys. Rev. Lett. **66**, 2285 (1991).
 - [19] H. Liu, proceedings of Quark Matter 2009.
 - [20] I. Abt *et al.* (HERA-B Collaboration), Eur. Phys. J. C **60**, 525 (2009) [arXiv:0812.0734 [hep-ex]].
 - [21] R. Vogt, Phys. Rev. C **61**, 035203 (2000) [arXiv:hep-ph/9907317].
 - [22] P. L. McGaughey, Nucl. Phys. A **610**, 394c (1996).
 - [23] P. Hoyer, M. Vanttinen, and U. Sukhatme, Phys. Lett. B **246**, 217 (1990).
 - [24] A. D. Frawley, private communication.
 - [25] B. Alessandro *et al.* (NA50 Collaboration), Eur. Phys. J. C **48**, 329 (2006); **33**, 31 (2004).
 - [26] R. Vogt, Phys. Rept. **310**, 197 (1999).
 - [27] C. Lourenço, R. Vogt and H. Wöhri, JHEP **0902**, 014 (2009) [arXiv:0901.3054 [hep-ph]].
 - [28] K. J. Eskola, V. J. Kolhinen and P. V. Ruuskanen, Nucl. Phys. B **535**, 351 (1998) [arXiv:hep-ph/9802350].
 - [29] K. J. Eskola, V. J. Kolhinen and C. A. Salgado, Eur. Phys. J. C **9**, 61 (1999) [arXiv:hep-ph/9807297].
 - [30] D. de Florian and R. Sassot, Phys. Rev. D **69**, 074028 (2004) [arXiv:hep-ph/0311227].
 - [31] M. Hirai, S. Kumano and T. H. Nagai, Phys. Rev. C **70**, 044905 (2004) [arXiv:hep-ph/0404093].
 - [32] P. Charpentier *et al.* (NA3 Collaboration), Z. Phys. C **20**, 101 (1983).
 - [33] D. M. Alde *et al.* (E772 Collaboration), Phys. Rev. Lett. **66**, 2285 (1991).
 - [34] S. Gavin and M. Gyulassy, Phys. Lett. B **214**, 241 (1988).

- [35] J. Hüfner, Y. Kurihara, and H. J. Pirner, Phys. Lett. B **215**, 218 (1988); J.-P. Blaizot and J.-Y. Ollitrault, Phys. Lett. B **217**, 392 (1989).
- [36] T. Ullrich, J. Phys. G **35**, 104041 (2008).
- [37] M. Gluck, E. Reya and A. Vogt, Z. Phys. C **53**, 127 (1992).
- [38] *et al.* (PHENIX Collaboration), Phys. Rev. C **77**, 024912 (2008) [arXiv:0711.3917 [nucl-ex]]; erratum arXiv:0903.4845 [nucl-ex].
- [39] R. Vogt, J. Phys. G **31**, S773 (2005) [arXiv:hep-ph/0412303].
- [40] A. J. Baltz *et al.*, Phys. Rept. **458**, 1 (2008) [arXiv:0706.3356[nucl-ex]].
- [41] K. J. Eskola, H. Honkanen, V. J. Kolhinen, J. w. Qiu and C. A. Salgado, Nucl. Phys. B **660**, 211 (2003) [arXiv:hep-ph/0211239].
- [42] K.J. Eskola, V.J. Kolhinen and R. Vogt, Phys. Lett. B **582** (2004) 157 [arXiv:hep-ph/0310111].
- [43] A. Dainese, R. Vogt, M. Bondila, K.J. Eskola and V.J. Kolhinen, J. Phys. G **30**, 1787 (2004) [arXiv:hep-ph/0403098].
- [44] Heavy Quarks, Summary Report for the HERA-LHC Workshop Proceedings, J. Baines *et al.*, arXiv:hep-ph/0601164.
- [45] D. Kharzeev, E. Levin, M. Nardi and K. Tuchin, arXiv:0809.2933 [hep-ph].
- [46] R. Vogt, Phys. Rev. C **71**, 054902 (2005) [arXiv:hep-ph/0411378]; Heavy Ion Phys. **25** (2006), 97 [arXiv:nucl-th/0507027].
- [47] R. L. Thews and M. L. Mangano, Phys. Rev. C **73**, 014904 (2006) [arXiv:nucl-th/0505055].
- [48] T. Kitigaki *et al.* (E745 Collaboration), Phys. Lett. B **214**, 281 (1988).
- [49] S. R. Klein and R. Vogt, Phys. Rev. Lett. **91**, 142301 (2003) [arXiv:nucl-th/0305046].
- [50] K. Adcox *et al.* (PHENIX Collaboration), Phys. Rev. Lett. **88**, 022301 (2002) [arXiv:nucl-ex/0109003].
- [51] D. Kharzeev, E.M. Levin and M. Nardi, arXiv:hep-ph/0212316; L. Hulthen and M. Sagawara, *Handbüch der Physik*, **39** (1957).